

Control of alveolar macrophage differentiation by Siah1a/2 ubiquitin ligases limits carcinogen-induced lung adenocarcinoma

Marzia Scortegagna^{1^}, Yuanning Du¹, Linda M. Bradley¹, Kun Wang², Eytan Rupp², Rabi Murad¹, Ze'ev A. Ronai^{1^}

¹NCI designated Cancer Center @ Sanford Burnham Prebys Medical Discovery Institute, CA, 92037 and ²Cancer Data Science Lab (CDSL), National Cancer Institute, National Institute of Health, Bethesda, MD 20892

^Correspondence: Ze'ev Ronai zeev@ronailab.net or Marzia Scortegagna mscortegagna@sbpdiscovery.org
Sanford Burnham Prebys, Medical Discovery Institute, 10901 N. Torrey Pines Rd. La Jolla, CA, 92037, USA.

Keywords: Siah1a, Siah2, macrophages, alveolar macrophages, lung cancer, urethane, lung adenocarcinoma, β -catenin, NRF2.

Abstract

Tumor microenvironment components, including T and myeloid cells, play important roles in lung adenocarcinoma (LADC) progression and response to therapy. Here, we identify a role for Siah1a/2 ubiquitin ligases in controlling alveolar macrophage (AM) differentiation and urethane-induced LADC. Genetic ablation of Siah1a/2 in AMs enriched their immature state, coinciding with increased pro-tumorigenic and inflammatory gene signatures and abundance of Siah1a/2 substrates NRF2 and β -catenin. Urethane administration to mice enriched the population of monocytic and immature-like AMs, which were more prevalent in the lungs of mice carrying Siah1a/2-ablated macrophages. While resembling transitional profibrotic macrophages often seen in lung fibrosis, enrichment of immature AMs coincided with the development of more frequent and larger lung tumors in urethane-treated mice harboring Siah1a/2 ablated macrophages compared with controls. Gene expression signature of Siah1a/2 ablated immature-like AMs is associated with increased infiltration of CD14⁺ immune cells and worse survival of LADC patients. Our findings identify Siah1a/2 as gatekeepers of cancer development by controlling AM differentiation and profibrotic phenotypes contributing to carcinogen-induced lung cancer.

Introduction

Our understanding of how the immune system controls tumor development, progression, and therapy response has prompted development of therapies to modify and exploit select immune system components^{1,2}. Complex immune system/tumor cross-talk is in part mediated by tumor microenvironment (TME) components, now known to be important determinants of immune cell activation and infiltration. Specific immune cell components, including cytotoxic and regulatory T cells and dendritic cells, function in the TME and are implicated in T cell infiltration and activation and therefore in control of tumor growth³⁻⁴. Other TME components include fibroblasts and endothelial cells^{5,6} as well as macrophages, which are less studied myeloid cells recently recognized as controlling tumor growth^{7,8}. Here we focus on the role of macrophages in lung cancer development using a unique genetic model in which the ubiquitin ligases *Siah1a/2* are ablated in macrophages.

Approximately 85% of lung cancers are non-small cell lung cancer (NSCLC), with lung adenocarcinoma (LADC) and squamous cell carcinoma the most common subtypes⁹. In response to chemical carcinogens (i.e., urethane), mice develop pulmonary adenocarcinoma resembling human adenocarcinoma harboring *KRAS* mutations¹⁰. Several studies have reported the importance of the lung microenvironment, including immune system components, in lung cancer development, and many highlight the abundance of macrophages and their possible contribution to its development^{11,12}. Two macrophage populations, alveolar macrophages (AMs) and interstitial macrophages (IMs), are abundant in normal lung: AMs are in close contact with type I and II epithelial cells in alveoli, while IMs are found in parenchyma between the vascular endothelium and the alveolar epithelium^{13,14}. AMs are derived from fetal monocytes that populate alveoli soon after birth and self-renew independently of bone marrow contribution^{15,16}. Fetal monocytes accumulate in the developing mouse lung at E14.5 and differentiate into immature (F4/80⁺, CD11c⁺, CD11b intermediate, and SiglecF low) AMs^{17,18}. They then mature postnatally into AMs (CD11c⁺ F4/80⁺ SiglecF⁺ and CD11b low), a process requiring GM-CSF-PPRγ signaling¹⁶. After inflammatory insult, bone marrow-derived cells can differentiate into AMs¹⁶. Notably, microenvironmental factors, including oxygen tension, glucose supply, and exposure to surfactant-rich fluid, all of which fluctuate during acute infection or chronic inflammation, as well as communication with alveolar epithelial cells, define AM development and function^{19,20}. Relevant to cancer, previous studies identified correlations between density of tumor-associated macrophages (TAMs), their abundance in stroma, and M2 polarization with worse patient survival^{12,11}. Of note, AMs obtained by bronchoalveolar lavage from patients with lung cancer exhibit reduced phagocytic capabilities²¹, although their role in lung cancer progression is still debated. This study extends our earlier analysis of *Siah2* in anti-tumor immunity. *Siah2* mutant mice show decreased melanoma tumor growth, an

outcome most notable in the context of immunogenic melanomas. Mechanistically, Siah2 reportedly regulates activity of T cells, primarily Tregs, by controlling their proliferation and infiltration of melanoma tumors²². Likewise, treatment of *Siah2*^{KO} mice with anti-PD1 therapy effectively blocked development of therapy-resistant (“cold”) melanoma²². These observations established the importance of Siah2 in the TME and extended earlier studies that established Siah2 importance in tumor-intrinsic functions. Previously, in analyzing melanoma infiltration by immune cells we developed Siah2 KO mice and identified enrichment of macrophage subpopulations. Here we analyzed Siah1a/2 function in macrophages by conditionally ablating Siah1a/2 genes in macrophage cells. Mice deficient in Siah1a/2 in macrophages harbored AMs in an immature-like state, and those cells exhibited a unique inflammatory signature, which was enhanced in mice treated with the carcinogen urethane. Urethane-treated mice also exhibited more frequent and larger lung tumors than WT controls, suggesting that Siah1a/2 serve as gatekeepers of macrophage ability to control lung cancer development.

Results

Siah1a and Siah2 are required for AM terminal differentiation and maturation

To establish mice with conditional loss of Siah1a and Siah2 (*Siah1a/2*) in myeloid cells, we generated *Siah1a*^{ff}::*Siah2*^{ff} mice and then crossed them with macrophage-specific Cre (*Lyz2*^{Cre}) mice, to ablate Siah1a/2 in macrophages (*cSiah1a/2*^{ff}::*Lyz2*^{Cre}). We then characterized macrophages in spleen, heart, and kidney of *cSiah1a/2*^{ff}::*Lyz2*^{Cre} and WT mice focusing on CD45⁺ cells enriched for MØ markers (CD11b⁺ and F480⁺). We observed that the frequency of these cells in each organ was comparable in both genotypes (Sup. Figure 1A).

We next used markers of MØ subtypes to FACS-sort and characterize AM and IM populations in mouse lung tissues. The overall % of either CD45⁺ cells or of IMs (CD11b⁺ F4/80⁺) was comparable in lungs of both genotypes (Figure 1A and Sup. Figure 1B). However, Siah1a/2 loss in macrophages decreased AM (CD11b low F480⁺) frequency in lung relative to WT cells (Figure 1B, F). This decrease was further reflected in the fraction of mature AMs (CD11b low F4/80⁺ CD11c⁺ SiglecF⁺) (Figures 1C, 1F). These findings suggest that AMs are the primary MØ population whose differentiation requires Siah1a/2. Of note, most CD11b low F480⁺ cells were positive for the mannose receptor CD206⁺ in both WT and *cSiah1a/2*^{ff}::*Lyz2*^{Cre} genotypes (Sup. Figure 1C), confirming the high expression of CD206 in AMs.

Accordingly, in WT mice, most CD11b low F480⁺ cells were positive for other markers of mature AMs (SiglecF and CD11c); however, in *cSiah1a/2*^{ff}::*Lyz2*^{Cre} mice a smaller fraction was positive for mature macrophage

markers (Figure 1D). Correspondingly, the frequency of immature AMs (CD11b low F480⁺CD11c⁺ SiglecF⁺) in the AM population was 4 times higher in *cSiah1a/2^{ff}::Lyz2^{Cre}* relative to WT mice (Figure 1E).

Notably, in the mature (CD11b low F4/80⁺ CD11c⁺ SiglecF⁺) AM population from *cSiah1a/2^{ff}::Lyz2^{Cre}* mice, we observed a significant decrease in CD11c- and SiglecF-expressing cells and an increase in CD11b expression relative to that seen in WT mice (Figure 1G), confirming that *Siah1a/2*-deficient AMs exhibit a relatively immature-like phenotype compared to WT mice. Nonetheless, expression of F4/80, MHCI, CD80 and CD206 in AMs was comparable in macrophages from both genotypes (Sup. Figure 1D), suggesting that changes seen in CD11c and SiglecF expression in AMs reflect their differentiation status.

Decreased CD11c expression seen in *Siah1a/2*-deficient AMs coupled with knowledge that a subpopulation of IMs express CD11c pointed to the possibility that *Siah1a/2* affects CD11c⁺ IMs. Indeed, we observed that the frequency of CD11c⁺ IMs slightly but significantly decreased (43% of CD45⁺ cells in WT compared to 33% in *Siah1a/2*-deleted cells), while the frequency of CD11c⁻ IMs significantly increased among IMs from *cSiah1a/2^{ff}::Lyz2^{Cre}* compared to WT mice (Figure 1H). These changes did not alter CD206 frequency, and the expression of CD11c within the CD11c⁺ IM population was comparable in WT and *cSiah1a/2^{ff}::Lyz2^{Cre}* cells (Sup. Figure 1E). Importantly, we observed no changes in frequency of other immune cell populations, including neutrophils, CD4, CD8, or B cells, or monocytes, except for a significant decrease in NK1.1⁺ cells (Sup Figure 1F). Overall, these data suggest that *Siah1a* and *Siah2* are required for AM cell differentiation to a fully mature state.

To assess the relative contribution of each ligase to phenotypes described above, we generated mice in which a single *Siah* gene was ablated in macrophages (*Siah1a^{ff}::Lyz2^{Cre}* and *Siah2^{ff}::Lyz2^{Cre}*) and then subjected lungs from these mice to FACS analysis. AM frequency among CD45⁺ cells was comparable in mice harboring WT, *Siah1*- or *Siah2*-deficient macrophages, although we observed a slight but significant decrease of CD11c and SiglecF expression on AMs from *cSiah1a^{ff}::Lyz2^{Cre}* relative to WT mice and a slight but significant increase of SiglecF expression on AMs from *cSiah2^{ff}::Lyz2^{Cre}* relative to WT mice (Figure 1I and J). Notably, these differences were less pronounced than those seen in DKO (*cSiah1a/2^{ff}::Lyz2^{Cre}*) macrophages, suggesting that *Siah2* can augment changes triggered by *Siah1a* in AM. While the CD11b⁺ F480⁺ population was comparable among WT and *Siah1a*-depleted cells, we observed a slight but significant decrease of this population in *Siah2* depleted cells, when compared to WT. We also observed a slight but significant decrease in CD11c⁺ IMs, along with a similar decrease

in CD11c⁻ IMs among *cSiah1a^{ff}::Lyz2^{Cre}* as opposed to WT genotypes. (Sup figure 1 G). These data indicate that both Siah1a and Siah2 are necessary for AM maturation.

Lyz2 Cre-induced gene deletion can occur embryonically¹⁶. To determine whether phenotypes described here emerge pre- or post-natal, we performed comparable analysis in a mouse model in which Siah1/2 ablation is catalyzed by CD11c-Cre, a driver expressed in AMs at its highest levels after birth¹⁶. This approach allowed us to confirm Siah1a/2 function in maintenance of AM homeostasis and potentially exclude a cell-intrinsic role of Siah1a/2 in neutrophils (which also express *Lyz2*). Indeed, crossing of CD11c^{Cre} with *Siah1a^{ff}:Siah2^{ff}* mice ablated Siah1a and Siah2 in AMs, CD11c⁺ IMs and dendritic cells. As we observed in *Lyz2^{Cre}* mice, CD45⁺ cell frequency in lung was comparable in WT and mutant mice (Sup Figure 1H). Likewise, Siah1a/Siah2 ablation via CD11C^{Cre} significantly decreased the frequency of AMs and CD11c⁺ IMs, while increased the frequency of CD11c⁻ IMs (Figure 1K, M). CD11c, SiglecF and CD206 expression also significantly decreased in AMs from *cSiah1a/2^{ff}::CD11c^{Cre}* compared to WT lungs (Figure 1L), phenotypes comparable to those seen in analysis using the *Lyz2* driver. Of interest, single deletion of Siah1a or Siah2 in CD11c⁺ cells did not alter frequency of AMs, CD11c⁺ IMs or CD11c⁻ IMs (figure 1K, M). Within the AM population, CD11c and CD206 expression was comparable in WT and Siah1a- or Siah2-deleted cells, while we observed a small but significant decrease in SiglecF expression in Siah1a-deleted relative to WT cells (Figure 1L). Here, by using a second mouse model, we confirmed the role of Siah1a/2 in AM maturation and differentiation.

Dendritic cell frequency or that of other immune cell populations (including CD4 or CD8 cells, neutrophils, or B cells) was comparable in WT and Siah1a or Siah2 singly- or doubly-deleted cells (Supplemental Figure I). We also confirmed a significant decrease in frequency of NK1.1-positive cells seen in both *cSiah1a/2^{ff}::Lyz2^{Cre}* and in *cSiah1a/2^{ff}::CD11c^{Cre}* CD45⁺ cells of the lungs (Sup. Figure 1J), suggesting that Siah1a and Siah2 expression in the myeloid population is responsible for NK1.1 cell recruitment.

Siah1a and Siah2 regulates AM maturation of fetal monocytes to AMs.

To determine the possible role of Siah1a/2 in development of fetal to mature AMs we analyzed AM development at E17.5 but observed no differences in frequency of immature (F4/80^{int} and CD11b^{int}) AMs in WT and Siah1a/2-deleted cells (Figure 2A). CD11b and F4/80 expression levels on immature AMs were comparable in *cSiah1a/2^{ff}::Lyz2^{Cre}* and WT cells, but CD11c expression was significantly decreased in *cSiah1a/2^{ff}::Lyz2^{Cre}* immature AMs relative to WT cells, suggesting a differentiation delay (Figure 2B). At birth (day 0) the frequency

of CD11b low and F480⁺ cells was comparable in WT and *cSiah1a/2^{ff}::CD11c^{Cre}* lungs (Figure 2C), but the frequency of CD11c⁺ SiglecF⁺ was markedly decreased in *Siah1a/Siah2*-deleted CD11b low F480⁺ cells relative to WT (Figure 2C, F). Within the population of *Siah1a/2*-deleted AMs (CD11b low F480⁺ SiglecF⁺ CD11c⁺ cells) we observed a significant decrease in CD11c and SiglecF expression relative to WT cells but observed no difference in F4/80 expression between genotypes (Figure 2D, F). We also observed an increased frequency of CD11c⁻ IMs and a decreased frequency of CD11c⁺ IMs (Figure 2E). These data suggest that *Siah1a/Siah2* deletion does not change the frequency of fetal lung monocyte-derived pre-AMs but rather blocks their full maturation, based on decreased CD11c and SiglecF expression.

AM regeneration from bone marrow requires *Siah1a* and *Siah2*

At steady state AMs self-renew while in inflammatory conditions or following bone marrow transplant, bone marrow-derived monocytes can replenish the AM population in the lung^{23,24}. To assess *Siah1a/2* activity in bone marrow-derived AMs, we established a BM chimeric mouse model in which BM cells from *Lyz2^{Cre}* or *cSiah1a/2^{ff}::Lyz2^{Cre}* CD45.2⁺ mice were co-transferred with CD45.1⁺ cells into irradiated recipient mice. Then, 8 weeks later, we collected lungs from recipients and subjected cells to FACS analysis. Gating of mature AMs (CD11c⁺ SiglecF⁺ CD11b low and F480⁺) for CD45.1- and CD45.2-positive cells revealed that 70% of AMs were reconstituted with CD45.2⁺ WT cells, while only 50% of AMs were reconstituted with CD45.2⁺ and *Siah1a/2*-depleted cells (Figures 3A and 3B). Notably, CD11c and SiglecF expression significantly decreased within CD45.2⁺ *Siah1a/2*-depleted AMs, while of F4/80 expression was unchanged, suggesting inhibition of AM maturation (Figure 3C). Moreover, while 37% of CD11c⁺ IMs were reconstituted with CD45.2⁺ WT cells, ~30% of CD11c⁺ IMs were reconstituted with CD45.2⁺ *Siah1a/2*-depleted cells (Figure 3D). Given that CD11c⁻ IMs and other immune cell components (monocytes, neutrophils, CD4 or CD8 cells) were equally represented in CD45.2⁺ WT and *Siah1a/2*-depleted cells (Figure 3E), we conclude that *Siah1a/2* activity primarily impacts BM-derived AMs and CD11c⁺ IMs. As confirmation, we repeated the mixed bone marrow experiment using the *CD11c Cre* line. As in the *Lyz2 Cre* line, ~70% of AMs were reconstituted with CD45.2⁺ WT cells, while only 30% of AMs were reconstituted with CD45.2⁺ *Siah1a/2* depleted cells (Supp. Figure 2A). Within the CD45.2⁺ AM population CD11c expression significantly decreased in *Siah1a/2*-depleted relative to WT cells (Supp. Figure 2B), while we observed no differences in CD11c⁺ and CD11c⁻ IMs (Sup. Figure 2C). These data strongly suggest that *Siah1a* and *Siah2* function in maturation of AMs from bone marrow-derived monocytes.

Siah1a/2 controls immunoregulatory function of AMs under homeostatic conditions.

To assess changes in gene expression and signaling pathways in AMs following *Siah1a/2* depletion we performed RNA-seq analysis of lung cells (n=3 for WT and KO, n=1 for *Cd11c* three lungs per sample) sorted by FACS based on *CD11c*⁺ *F480*⁺ *SiglecF*⁺ expression from WT, *cSiah1a/2^{ff}::Lyz2^{Cre}* and *cSiah1a/2^{ff}::CD11c^{Cre}* mice. Principal components analysis showed a similar gene expression patterns of samples from *cSiah1a/2^{ff}::Lyz2^{Cre}* and *cSiah1a/2^{ff}::CD11c^{Cre}* mice, as well as a distinct segregation between WT and *Siah1a/2*-depleted macrophages along main component PC1 (Figure 4A). Differential gene expression analysis confirmed similar gene expression signatures in AMs from *cSiah1a/2^{ff}::Lyz2^{Cre}* and *cSiah1a/2^{ff}::CD11c^{Cre}* mice and a reduced expression of *Siah1a* and *Siah2* in *Siah1a/2*-deleted AMs (Figure 4B). Relative to WT AMs, we identified 565 upregulated and 363 downregulated genes distinctly expressed in AM samples from *cSiah1a/2^{ff}::Lyz2^{Cre}* mice (Figure 4B, Sup Figure 3A). Given both the immature-like state of AMs from *Siah1a/2*-depleted MΦ and the importance of GMCSF/PPARγ signaling in AM differentiation and maturation, we asked whether components of these pathways (namely, GMCSF (*Csf2*), *Tgfb1*, *Bach2*, *Tgfb1*, *Tgfb2*, *Csf2ra*, and *Csf2rb*) were differentially expressed. Except for a small but significant increase in *Csf2rb* and *Tgfb2* expression seen in *Siah1a/2*-depleted macrophages, expression of all other GMCSF components or their downstream effectors (PPARγ) was comparable among genotypes (Sup. Figure 3B).

To identify pathways deregulated by *Siah1a/2* ablation, we performed pathway analysis using IPA of the above differentially expressed gene. Among the most activated signaling pathways were tumor microenvironment, actin cytoskeleton and NRF2 (Figure 4C). NRF2 is tightly regulated at transcriptional and post-translational levels, with its key guardian, KEAP1, controlling its stability^{25, 26, 27}. Notably, under hypoxic or low glucose conditions *Siah2* has been implicated in control of NRF2 stability^{28, 29}. Accordingly, we observed induction of NRF2-target genes, including those involved in diverse metabolic activities, NADPH production, and the immune response, in samples from *Siah1a/2*-deficient relative to WT AMs (Figure 4D). Moreover, Western blot analysis of primary AM cultures from lungs of these mice, confirmed a marked increase in levels of NRF2 protein (Fig 4E) (but not mRNA (Fig 4F) and a corresponding increase in mRNAs encoding NRF2 targets, including *Ftl1*, *Hmox1*, and *Vegfa* in *cSiah1a/2^{ff}::Lyz2^{Cre}* AMs when compared to WT (Figure 4F). At the same time, immunofluorescence revealed comparable nuclear localization of PPARγ in AMs from both genotypes, excluding relevance of the PPARγ pathway to *Siah1a/2* activity in this context (Sup. Figure 3C). Of note, differences in NRF2 levels and those of its target genes were restricted to AMs and not seen in BM-derived macrophages (Sup figure 3D).

We next addressed mechanisms underlying upregulation of cytoskeletal signaling seen in Siah1a/2-deficient AMs (Figure 4C). Among Siah2 substrates that could be implicated in its control of cytoskeletal organization and cell migration is β -catenin^{30, 31, 32}. β -catenin is also implicated in AM differentiation³³, as it drives immature-like phenotypes similar to the one observed in Siah1a/2- ablated AMs. Indeed, isolated AMs lacking Siah1a/2 showed increased nuclear localization of β -catenin, indicative of activation (Figure 4G). Moreover, immunohistochemistry with an antibody specific for the active form of β -catenin showed more nuclear and cytoplasmic intense staining in primary cultures of Siah1a/2-deficient compared to WT AMs (Supp Figure 3E). Activation of beta catenin in macrophages was found to potentiate STAT3 activity^{34, 35, 36}. Accordingly, qPCR analysis of primary AM cultures confirmed a marked increase in expression of β -catenin targets and STAT3 targets, including Axin2, Serpine1, Mmp2, Fizz1 and Chil3 (Figure 4H). Likewise, IPA analysis of RNA-seq data revealed increased transcription of β -catenin- and of STAT3-activated genes, including metabolic signaling factors (glycolysis) linked with β -catenin activation, in Siah1a/2- ablated AMs that are maintained under a homeostatic state when compared to WT (Figure 4I, J). Independent support for a link between Siah1a/2 and a unique inflammatory signature observed in AMs comes from the identification of a gene signature reported in lungs of mice subjected to bleomycin treatment, a chemical widely used to induce lung fibrosis (Figure 4I). Of note, during bleomycin induced fibrosis β -catenin activity is increased in alveolar macrophages³⁷ and mice with conditional β -catenin knockdown driven by the CD11c promoter show improvement in fibrosis after bleomycin treatment³³. Overall, these data reveal that Siah1a/2 deletion in AMs increases NRF2 and beta catenin signaling, and that Siah1a/2-deleted AMs display a profibrotic immune signature associated with tumor progression (Figure 4 D and I).

Siah1a and Siah2 deletion in macrophages promotes urethane-induced lung cancer

Given AM abundance in normal lung, we asked whether Siah1a/2 expression in AMs alters the course of lung cancer by subjecting mice harboring either WT or Siah1a/2-deficient AMs to treatment with urethane, a carcinogen that induces KRAS mutations and promotes lung tumor development³⁸. Lungs were collected from mice 24 weeks after the first of six weekly urethane injections. Notably, mice lacking Siah1a/2 in AMs showed increased numbers of tumor nodules (Figure 5A) and increased tumor size (Figure 5B), based on comprehensive assessment of serial lung sections (Figure 5C). While the frequency of CD45⁺ cells was comparable between genotypes (Supp. Figure 4A), AM frequency was lower in tumor-bearing mice (12% of CD45⁺ cells, Figure 5D) compared to tumor free mice (22% of CD45⁺ cells Figure 1C), with the most notable decrease observed in tumor bearing Siah1/2 deleted AMs (4% of CD45⁺ cells, Figure 5D). Of note, immature-like AMs, not observed in WT

tumor free mice (Figure 1E, F), were observed in WT after urethane administration, with the greatest increase seen among *Siah1a/2*-ablated AMs (Figure 5D, 5E, 5F). Among mature (*SiglecF*⁺ *CD11c*⁺ *F480*⁺ *CD11b*⁻) AMs population, *Siah1a/2*-deleted AMs exhibited a significant decrease in expression of *CD11c* (67%), *SiglecF* (36%) and the co-stimulatory protein *CD80* (80%) relative to WT after urethane administration, while the expression of *CD206* and *MHCI* was comparable (Figure 5G, Sup. Figure 4B). We also observed a small but significant increase in the number of *CD11c*⁻ IMs and a decrease in *CD11c*⁺ cells (Figure 5H and I), as seen in tumor-free mice. *Siah1a/2*-deficient IMs (*Lyz*^{Cre}) exhibited comparable levels of *MHCI*, *CD206*, *CD11c* and *CD80* within *CD11c*⁺ IMs to that seen in WT cells (Sup Figure 4C), suggesting that both genotypes exhibit similar degree of activation despite the lower frequency of *CD11c*⁺ IMs seen after *Siah1a/2* depletion. While there were no differences in the number of B cells or *CD4* and *CD8* cells, we observed a marked decrease in *CD44*⁺ cells within the *CD8* population, along with a lower frequency of *NK1*-positive and active (*B220*⁺ among *NK1.1*⁺) *NK1*⁺ cells after *Siah1a/2* ablation (*Lyz2*^{Cre}) relative to WT cells (Sup. Figure 4D).

***Siah1a/2* deletion in macrophages promotes a pro-fibrotic phenotype.**

To identify signaling pathways in immune cells altered by *Siah1a/2* deletion in lung macrophages, we performed single cell RNAseq (scRNA-seq) of *CD45*⁺ cells enriched from lungs collected from WT (n=1, pool of 3 lungs) and tumor-bearing mice (n=1, pool of 3 lungs) at the end of 6 weeks of urethane treatment. Integrated analysis of WT (n=7884 cells) and KO (n=6035 cells) scRNA-seq datasets identified 17 immune cell clusters with distinct gene expression patterns (Figure 6A and 6B). Of these 17 clusters, clusters 1 and 13 were positive for *Ncr1* and *Klrb1a*, markers of NK cells; cluster 12 was positive for the neutrophil marker *Csf3r*; cluster 15 expressed B cell markers *Cd19* and *Pax5*; and clusters 0, 4, 6, 7, 8 and 10 expressed the T cell marker *Cd3e*. The myeloid population expressing *Csf1r* was represented by clusters 2, 3, 5 and 11. We identified plasmacytoid dendritic cells (DCs) in cluster 9 (*Cd209a*, *Itgax*, *H2-aa*), while DCs were also identified in cluster 16 (*H2-aa*, *Flt3* and *Ly75*), and basophils (*Fcer1a* and *Cd200r3*) in cluster 14 (Figure 6B).

Within T cell populations, *CD8*⁺ cells were distributed in 3 clusters: cluster 0, which included terminally effector exhausted *CD8*⁺ cells expressing genes involved in anti-tumor immunity like *Ifnγ* and *Nkg7*, and genes with immunosuppression function like *Lag3*, *Klrc1*, and *Ctla4*; cluster 6, consisting of *CD8*⁺ effector T cells expressing *Ifnγ* and the interferon response genes *Ifi208* and *Ifit3*; and cluster 10, representing proliferating effector *CD8*⁺ cells expressing *Mki67* and *Top2a*. Among *CD4*⁺ populations, cluster 7 consisted of *CD4*⁺ effector cells producing

Ifn γ , while cluster 4 represented Foxp3-expressing CD4⁺ T regulatory cells. Cluster 8 included T cells negative for CD4 and CD8 and expressing Tcf7 and Lef1 (Figure 6B).

Changes in immune cell frequencies in *Siah1a/2*-ablated AMs included a notable increase in neutrophils represented in cluster 12 (2.45% in *cSiah1a/2^{ff}::Lyz2^{Cre}* cells vs 1.15% in WT cells) concomitant with a decrease in CD8 effector/proliferative cells represented in cluster 10 (2.93% in *cSiah1a/2^{ff}::Lyz2^{Cre}* cells vs. 4.46% of WT cells, Sup. Figure 5A). Within the myeloid population of Csf1r⁺ cells (clusters 2, 3, and 5), cluster 2 exhibited the highest expression of Adgre1 (F4/80) and was enriched of cells positive for AM markers including Apoe, Mrc1 (CD206), Cd72 and Itgax (Figure 6B). This cluster was also positive for genes indicative of monocytic origin (Ly6c2, Fcgr1 and H2-a) and may represent monocytes differentiating into AMs (Figure 6B). Cells in cluster 3 expressed highest levels of Ly6c, indicative of monocytes, while cluster 5 was represented by macrophages expressing Hp, Ear2, Ace, Chil3 and Fn1 (Figure 6B).

Among upstream regulators, IPA analysis identified significant upregulation of β -catenin signature genes and bleomycin-induced genes (profibrotic genes) (Figure 6C) in cluster 2, which contained residential and monocyte-derived AM populations. Among these, were genes known to be involved in tumor progression, (Ccl6, Ccl9, Vegfa, Anxa2 and Lgals3) (Figure 6C). *Siah1a/2*-deleted cells of cluster 2 also showed increased expression of glycolysis-associated genes relative to WT, suggestive of increased of macrophage activity and associated to a pro-fibrotic phenotype in AMs³⁹ (Figure 6D). Differential gene expression of cluster 5 exhibited increased mitochondrial respiration in *Siah1a/2* deleted cells and an increased expression of Fn1 (Sup. Figure 5B). Macrophages possessing an immature-like phenotype were enriched upon *Siah1a/2* ablation in cluster 2, as reflected by increased Itgam (CD11b) expression concomitant with decreased Itgax (CD11c) and Cx3cr1 expression (Figure 6E). Notably, *Siah1a/2*-deleted monocytes (cluster 3) exhibited increased expression of β -catenin-activated genes (i.e., Plaur, Fn1 and S100a4) and profibrotic genes (bleomycin induced genes), which are implicated in lung fibrosis (Figure 6F).

Although we observed increased NRF2 activity in tumor free lungs, as evidenced by Hmox1, Ftl1 or Fth1 upregulation in *Siah1a/2*-ablated WT AMs, we did not observe these increases after urethane treatment, likely since urethane induces an oxidative /inflammatory phenotype that may mask effects of *Siah1a/2*-depletion (Sup Figure 5C). Consistently, U-map analysis revealed high expression of NRF2 in both WT and *Siah1a/2* deleted myeloid population (Sup. Figure 5C) indicative of urethane-induced oxidative stress^{40,41} which led to increased

NRF2 expression and activity. Of note, the inflammatory signature seen in *Siah1a/2*-deficient AMs in tumor-free lungs was maintained in tumor-bearing lungs (Figure 6C). Accordingly, AMs presenting an immature-like state reportedly exhibit a unique inflammatory signature in pathologies similar to that seen in fibrotic macrophages^{23, 42, 43}.

Initial analyses of the 3 myeloid clusters (2, 3, 5) did not separate residential AMs from monocytes derived AMs. Re-clustering of those 3 groups (Figure 6A) gave rise to 9 myeloid subclusters (Figure 7A). All expressed genes associated with monocytic origin (*Ccr2*, *Cx3cr1*, *Ly6c2*, *H2-aa* and *H2-ab1*; Figure 7B). Among the 8 subclusters, 1, 2, and 3 exhibited highest *Ly6c2* and *Sell* expression, a characteristic of monocyte populations. Subcluster 3 also exhibited highest expression of *Hp* and *Fn1*. Subclusters 5, 6, 7, and 8 showed lowest *Ly6c2* and *Ccr2* expression, indicating they contain more differentiated residential macrophages (Figure 7C). Subclusters 5 and 8 exhibited AM markers (*Itgax*, *Mrc1*, *Apoe* and *Siglec1*), reflective of a mature state. By contrast, subcluster 4 was CD3e-positive, indicating a unique group of T cells also positive for F4/80 and CD11c (Figure 7C). Lastly, subcluster 0 was positive for markers of monocytic origin (*Ly6c2*, *Ccr2* and *H2-aa*) and for AM markers (*Itgax*, *Mrc1*, *Apoe*, *Cd74*, *Cxcl16* and *Cd72*, which were also found in subcluster 5), suggesting that cluster 0 contains immature AM of monocytic origin. Of note, while subclusters 5 and 8 showed highest expression of immunosuppressors (*C1qa*, *C1qb* and *C1qc*), subcluster 0 showed intermediate levels of those genes, confirming the transition state of cluster 0 cells (Figure 7C).

Decreased proportions of AMs in subclusters 5, among CD45⁺ cells from lungs of *Siah1a/2*-depleted macrophages (Supp Figure 6A) compared to WT, confirmed our earlier FACS analyses. Likewise, the immature-like state of AM in cluster 0 was confirmed by gene expression analysis showing increased *Itgam* and decreased *Itgax* and *Cx3cr1* expression in *Siah1a/2*-depleted macrophages (Figure 7D). Lastly, increased expression of genes implicated in glycolysis (Supp. Figure 6B), a metabolic reprogramming found in pro-fibrotic AMs³⁹, along with increased β -catenin signaling and bleomycin induced genes was confirmed in *Siah1a/2*-depleted macrophages (Figure 7E). These data indicate that *Siah1a/2* loss in AM promotes pro-tumorigenic and pro-fibrotic phenotypes. Further analysis excluded the possibility that the immature-like state of *Siah1a/2*-deleted AMs was due to dysregulated recruitment of bone marrow-derived monocytes. Specifically, LY6C protein expression in AMs, immature AMs and IMs (Sup. Figure 6C) was comparable in WT and *Siah1a/2*-mutant cells, although we noted differences between IM and AM populations: LY6C was highest in CD11b⁺ F480⁺ CD11c⁻ and *SiglecF*⁻ cells (immature AMs) and in CD11c⁻ IMs and lowest in mature AMs (10%). These data suggest that immature-like

phenotypes seen in *Siah1a/2*-deleted AMs result from cell-autonomous effects rather than from impaired lung infiltration by monocytes.

To assess the possible clinical relevance of these findings, we determined the expression of genes that were significantly upregulated (65 genes) in cluster 0 (immature AMs) of *Siah1a/2* deleted cells (compared to WT; Supplemental Table 1) in two independent data sets. First, the expression of these 65 genes in TCGA database of LUAD (lung adenocarcinoma) cohort identified patients with poor prognosis and shorter survival (Figure 7F). Second, using a precomputed estimates of cell abundance or cell-type-specific signature based on deconvolving cell-type-specific gene expression in each sample from bulk expression⁴⁴ of LUAD patients, patients with higher average expression of the unique signature (65 genes) identified in *Siah1a/2* ablated macrophages were also found to have increased myeloid cells (CD14⁺) infiltration (Figure 7G). The TCGA dataset of the LUAD was also used to identify which of the 65 genes are associated with worse survival. To this end, we calculated the hazard ratios for each of the 65 inflammatory genes that were significantly upregulated in cluster 0 (immature AMs of *Siah1a/2* mutant versus WT cells) identifying genes involved in glycolysis (i.e., lactate production and export *LDHA*, *SLC16A3*), in generation of plasmin and degradation of extracellular matrix (*PLAUR*, *S100A10/ANXA2*, *CTSL*, *ADAM8*) (Sup. Figure 7D). Of note, these signaling pathways have been observed in pro-fibrotic macrophages and implicated in cancer progression. Overall, these data establish the relevance of our finding in the urethane-induced lung cancer mouse model to human tumors.

Discussion

We report here that *Siah1a* and *Siah2* loss in AMs promotes their immature-like state and emergence of a profibrotic gene signature. Moreover, we show that *Siah1a* and *Siah2* activity likely enables alveolar macrophage differentiation and thus impacts lung inflammation. Selective ablation of *Siah1a* and *Siah2* in macrophages was performed using two complementing genetic approaches: the *Lyz2*-Cre and the *CD11c*-Cre models. While each system shows some cell type selectivity, both are expressed in AMs, supporting our conclusion that inflammatory phenotypes seen after *Siah1a/2* ablation by either system are primarily due to AMs activity. Using both approaches we define the role of *Siah1a* and *Siah2* in the shift of AMs from mature to an immature and pro-inflammatory phenotype, which was most pronounced following lung carcinogen administration. Mechanistically, we show that two substrates destabilized by *Siah1a/2*, NRF2 and β -catenin, mediate pro-tumorigenic phenotypes, suggesting that *Siah1a/2* ubiquitin ligases prevent inflammatory and profibrotic signaling by limiting NRF2 and β -catenin availability and activity. Notably, *Siah1a/2* effects were mainly

restricted to AMs, the most abundant population of lung macrophages. While AMs reportedly function in turnover of pulmonary surfactants and removal of dead cells from alveoli, their differentiation is thought to be primarily regulated by GM-CSF/PPAR γ and TGF β signaling^{16,45}. Here we show that Siah1a/2 contribute to AM maturation independently of the GM-CSF/PPAR γ pathways, revealing an unexpected signaling path underlying AM maturation.

NRF2 controls central cellular homeostatic pathways regulating reactive oxygen species, cellular redox, ferroptosis, apoptosis and key metabolic pathways⁴⁵. Notably, NRF2 undergoes extensive post-translational modifications that dictate its stability and activity, primarily by KEAP1. Regulation by Siah1a/2 represents a novel layer of NRF2 regulation likely in response to stress signaling, such as oxygen or glucose deprivation, activities often associated with Siah1a/2 function. Here we show that increased NRF2 protein level induces a set of target genes that are implicated in lung cancer progression, namely Arg1, VEGFA and HMOX1. The increased expression of these genes and others are conducive to cancer cells growth and proliferation.

β -catenin signaling reportedly modulates the immune response in macrophages, in part through STAT3-dependent IL4 signaling^{34, 35, 36}. In hepatocellular carcinoma, β -catenin activation in TAMs is linked with macrophage polarization to an M2 type³⁶. Likewise, increased β -catenin levels in AMs have been observed following treatment with the chemotherapy drug bleomycin³⁷, which promotes fibrosis. Notably, fibrosis is among the pathological condition enriched with immature-like alveolar macrophages^{23, 24, 42}.

Our findings in a lung carcinogen model confirm that Siah1a/2 controls AM differentiation and inflammatory signaling. Urethane induces pulmonary adenocarcinoma resembling human adenocarcinoma with KRAS mutations³⁸. We observed increased numbers of larger lung tumors in mice lacking Siah1a/2 in macrophages relative to controls. Siah1a/2 ablation increased the number of exhausted T cells and decreased the number of activated NK cells in lung tumors concomitant with increased expression of genes implicated in tumor proliferation and immunosuppression. Notably, while tissue-resident AMs self-renew at steady state, following infections or injury resident AMs are replaced by monocyte-derived AMs that differ from resident AMs phenotypically and metabolically. Immature AMs have been reported in several infections and lung pathologies, including fibrosis, but not yet in lung cancer. Here we demonstrate that during lung cancer the residential AM pool is replaced by monocyte-derived AMs exhibiting a profibrotic and immature-like state. Moreover, these cells exhibit an inflammatory signature distinct from residential AMs. In a lung cancer setting, Siah1a and Siah2 loss

enhances the immature state of monocyte-derived AMs and confers on them a unique profibrotic signature favoring lung cancer progression.

We also show that genes significantly upregulated in *Siah1a/2*-deleted immature-like AMs are associated with a poor survival in patient with lung adenocarcinoma. Notably, AI-based deconvolution of scRNAseq analyses of LUAD patients carrying the gene signature identified in the *Siah1a/2* ablated immature-like AMs revealed an association with higher infiltration of CD14⁺ myeloid cells and worse survival. This important observation implicates the monocytes/ macrophages infiltrated cell population in lung cancer progression. Among the genes upregulated in *Siah1a/2*-deleted immature-like AMs and associated with the highest significant hazard score were those involved in profibrotic macrophages. Consistent with our findings are reports implicating TAMs as important contributors to metabolism and matrix processing, which underlie lung cancer progression^{46, 47, 48, 49}. Along these lines, pulmonary fibrosis is a risk factor for developing lung carcinogenesis, and patients with idiopathic pulmonary fibrosis (IPF) later diagnosed with lung cancer tend to have a poorer prognosis than patients with lung cancer without IPF, regardless of treatment modality.

Overall, these studies indicate that *Siah1a/2* regulates AM differentiation and activity in a manner that controls immune cell recruitment and tumor growth. These findings could suggest new approaches to monitor or target specific macrophage populations, as means to antagonize lung cancer. Understanding molecular mechanisms underlying AM differentiation and control of lung cancer initiation and progression could offer better monitoring, stratifications and treatment options for patients with lung cancer.

Acknowledgements

We thank members of the Ronai lab for discussion and Shared Resources for various analyses (vivarium, FACS, bioinformatics) supported by P30CA030199 grant. Support by R35CA197465 to ZR is gratefully acknowledged.

Author contributions

MS and ZR designed the study. MS and YD performed the experiments. LB helped with immune study design and evaluation. RM, ER, KW performed bioinformatic analyses. MS and ZAR wrote the manuscript.

Conflict of Interest

ZAR is co-founder and scientist advisor of Pangea Biomed. No conflict of interest is reported for any of the other authors.

Material and Methods

Animals and tumor model

All experimental animal procedures were approved by the Institutional Animal Care and Use Committee of Sanford Burnham Prebys Medical Discovery Institute. *Siah1*^{ff} and *Siah2*^{ff} were generated by Cyagen. *Lyz2*^{Cre} and *CD11c*^{Cre} mice were purchased by Jackson. For the urethane-induced lung cancer model, mice were injected intraperitoneally with urethane (Sigma, 1mg/gr mouse) once a week for 6 weeks. Lungs were collected either 7 or 24 weeks after first urethane injection.

Bone marrow chimeras

C57Bl6 recipient mice were lethally-irradiated (1000 rads) and reconstituted by intravenous (i.v.) injection of 1×10^7 bone marrow (BM) cells isolated from femurs and tibias of donor *WT CD45.2*⁺, *cSiah1a/2*^{ff}::*Lyz2*^{Cre} *CD45.2*⁺ or *WT CD45.1*⁺ mice. Irradiated mice were injected intravenously with a 1:1 mixture of either *WT CD45.2*⁺ and *WT CD45.1*⁺ cells or *cSiah1a/2*^{ff}::*Lyz2*^{Cre} *CD45.2*⁺ cells and *WT CD45.1*⁺ cells for a total 1×10^7 BM cells. Recipients were treated with antibiotics (trimethoprim 8 mg/ml and sulfamethoxazole 40 mg/ml in drinking water) for 3 weeks after injection. Reconstitution was confirmed 6–8 weeks after BM transfer.

Tissue digestion

Tissues were excised, minced, and digested with 1 mg/ml collagenase D (Roche) and 100 µg/ml DNase I (Sigma) at 37°C for 45 minutes. Digests were then passed through a 70-µm cell strainer to generate a single-cell suspension. Cells were washed twice with PBS containing 2 mM EDTA and stained for flow cytometry.

Flow cytometry

Tissue-derived single-cell suspensions were washed twice with FACS staining buffer, fixed 15 min with 1% formaldehyde in PBS, washed twice, and resuspended in FACS staining buffer for staining with specific antibodies, followed by fixation with 1% formaldehyde and then flow cytometry analysis. The following antibodies were purchased from Biolegend: CD45.2 (104), CD8a (53-6.7), CD4 (GK1.5), CD45.1 (A20), CD11c (N418), CD11b (M1/70), MHC class I (AF6-88.5), CD80 (16-10A1), GR1 (RB6-8C5), CD206 (C068C2), F4/80 (BM8), SiglecF (S17007L), Ly6C (HK1.4), Ly6G (1A8), NK1.1 (PK136), B220 (RA3-6B2), CD44 (IM7). All data were collected on an LSRFortessa cell analyzer (BD Biosciences) and analyzed using FlowJo Software (Tree Star).

Histology and immunofluorescence

Lungs were fixed in 4% formalin overnight at 4°C, washed with PBS, paraffin-embedded, cut into 5 µm-thick sections and stained with H&E. For immunofluorescence, sections were deparaffinized, rehydrated and washed in PBS. Antigen retrieval was performed in a pressure cooker (Decloaking chamber, Biocare Medical) in citrate buffer (pH 6.0). Ki67 (AbCam Ab15580) immunostaining was performed by incubating sections overnight at 4°C with antibodies in Dako antibody diluent. Alexa Fluor 594-conjugated secondary antibodies was added for 1h at room temperature (Molecular Probes), and nuclei were counterstained using SlowFade Gold Antifade reagent (Vector) with 4',6-diamidino-2-phenylindole (DAPI, Vector). Image data were obtained using Olympus TH4–100 microscope and using Slidebook 4.1 digital microscopy. For quantification Ki67, positive cells were counted in ten random × 20 fields per mouse. Staining was scored by counting Ki67-positive relative to total cells.

Immunofluorescence

To stain AMs grown in culture, cells were grown on coverslips and fixed in fixation buffer (4% paraformaldehyde/2% Sucrose/PBS) for 20 min at room temperature. Coverslips were then rinsed twice in PBS and permeabilized in permeabilization buffer (0.4% Triton-X and 1% BSA in PBS) for 20 min. Primary antibodies were applied at 1:250 dilution in staining buffer (0.1% Triton-X and 0.1% BSA in PBS) overnight at 4°C in a humid chamber. Coverslips were washed 5 times (5-min each) in wash buffer (0.2% Triton-X and 0.2% BSA in PBS). Secondary antibodies (AlexaFluor secondary 488 or 594, Invitrogen) were applied at 1:250 dilution in staining buffer for 2-3 hours at room temperature in a humid chamber in the dark. Prior to mounting with Vectorshield with DAPI (Vector Laboratories, CA), coverslips were washed twice more in wash buffer. Immunofluorescent analysis was conducted on an Olympus TH4-100 fluorescent microscope using Slidebook V.4.1 digital microscopy.

Quantification of lung cancer

Fixed and embedded lung tissues were sliced to obtain five serial sections per lung. H&E staining was used to quantify number and size of nodules under a histology microscope. Size was calculated as the area of nodules using a measurement tool provided by CellSens Standard v3.2 software (Olimpus America).

AM primary cell culture

Lung tissue was digested as described above to obtain a single cell suspension. SiglecF-positive cells were isolated using anti-SiglecF microbeads (Miltenyi Biotec) and plated on non-treated 6-well plates in RPMI 1640 media

containing 1x Glutamax, 1x Pyruvate, 1x penicillin/Streptomycin, 10% FBS and 20 ng/ml of recombinant GM-CSF, based on a previous publication⁵⁰. After 16 hours media was replaced with fresh culture media, which was replaced with new media every 2 days. Cells were collected either the day after plating or after 6 days. When indicated, AMs were treated with 3uM XAV939 (Sigma) or 3uM ML385 (MedChem Express) overnight.

Bone marrow-derived cell culture

Mice were euthanized with CO₂, the femurs were removed, and BM cells were harvested and washed. For macrophage differentiation, BM cells were resuspended in RPMI-1640 medium containing 10% FBS, penicillin/streptomycin, and 2 mM L-glutamine and placed in Petri dishes. L929 cell supernatants (a source of macrophage-colony stimulating factor, M-CSF) were added at 30% (vol/vol), and cells were incubated 7 days. Differentiated macrophages were then harvested and used in the experiments.

Western blotting

Cells were washed once with PBS at room temperature and resuspended in RIPA buffer (PBS containing 1% NP-40, 1% sodium deoxycholate, 1% SDS, 1 mM EDTA, and phosphatase and protease inhibitors), while tissue was homogenized directly in RIPA buffer. Lysates were centrifuged, and supernatants were removed and subjected to SDS-PAGE. Proteins were transferred to nitrocellulose membranes (Osmonics Inc., MN, USA), which were blocked and incubated with respective primary antibodies followed by Alexa Fluor-conjugated or HRP-conjugated secondary antibodies. Blots were imaged using an Odyssey detection system (Amersham Bioscience, NJ, USA) or a ChemiDoc MP imaging system (BioRad).

RNA extraction and qRT-PCR analyses

Total RNA was extracted from tumors or cells using TRIzol (Ambion) and treated with DNase I. cDNA was synthesized using oligo-dT and random hexamer primers according to the SYBR Green qPCR protocol (Life Technologies). Total RNA was reverse transcribed using High Capacity Reverse Transcriptase kits (Invitrogen), according the manufacturer's protocol. RNA purity and concentration was checked and quantified by reading absorbance at 260 and 280 nm in a NanoDrop spectrophotometer (Thermo Fisher). qRT-PCR analyses were performed using SYBR Green RT-PCR kits (Invitrogen) on a Bio-Rad CFX Connect Real-Time system or Roche LightCycler. GAPDH or 18S served as internal control. PCR primers were designed using Primer3, and their specificity was checked using BLAST. PCR products were limited to 100–200 bp. Primer sequences are shown in Supplemental Table 2.

RNA-seq analysis

Lung tissues from mutant or WT mice were digested as described above, and CD11c⁺ SiglecF⁺ F4/80⁺ cells were sorted by flow cytometry and processed for gene expression analysis. PolyA RNA was isolated using the NEBNext® Poly(A) mRNA Magnetic Isolation Module, and bar-coded libraries were constructed using the NEBNext® Ultra™ Directional RNA Library Prep Kit for Illumina® (NEB, Ipswich MA). Libraries were pooled and sequenced single-end (1X75) on an Illumina NextSeq 500 using the High output V2 kit (Illumina Inc., San Diego CA). The RNA-seq samples were sequenced at a sequencing depth of 11-16 million reads.

Illumina Truseq adapters and polyA/polyT sequences were trimmed from raw reads using Cutadapt version 2.3⁵¹, Trimmed reads were aligned to mouse genome version mm10 and Ensembl gene annotations version 84 using STAR version 2.7.0d_0221⁵² adopting alignment parameters from ENCODE long RNA-seq pipeline (<https://github.com/ENCODE-DCC/long-rna-seq-pipeline>). RSEM version 1.3.1⁵³ was used to obtain gene level estimated counts and transcripts per million (TPM). FastQC version 0.11.5 (<https://www.bioinformatics.babraham.ac.uk/projects/fastqc/>) and MultiQC version 1.8⁵⁴ were used to assess the quality of trimmed raw reads and alignment to genome as well as transcriptome. To remove lowly expressed genes from downstream analysis, only genes with RSEM estimated counts equal or greater than 5 times the total number of samples were retained for differential expression analysis. Differential expression comparisons were performed using Wald test implemented in DESeq2 version 1.22.2⁵⁵. Genes with Benjamini-Hochberg corrected p-value < 0.05 and fold change ≥ 1.5 or ≤ -1.5 were identified as differentially expressed. Pathway analysis was performed in Ingenuity Pathway Analysis (Qiagen, Redwood City, USA).

Single-cell library preparation and sequencing

Mutant or WT mice were sacrificed 7 weeks after the first urethane treatment. Lungs were digested as described above. Single cell suspensions were washed with 1XPBS-4%FBS before incubation for 20 min on ice at 5×10^7 cells/ml with 500 ng/ml Fc block (2.4G2, BD Pharmingen). Cells were then incubated for 1 hour on ice with AF700 conjugated CD45.2 monoclonal antibody (104, Biolegend). For scRNA-seq libraries, DAPI negative (live) CD45⁺ cells were sorted using a flow cytometer, and sorted cells were resuspended in RPMI for counting. Libraries were prepared using Single Cell 3' Reagent Kits v3.1: Chromium™ Single Cell 3' Library & Gel Bead Kit v3.1, PN-1000196 and PN-1000129 and following the Single Cell 3' Reagent Kits v3 (PN-1000269) User Guide (Manual Part # CG000315 Rev C). Libraries were sequenced on NovaSeq S4, using half full lanes for 2 samples, with mean read depth of 87-128 thousand reads per cell.

scRNA-seq data pre-processing

10X Genomics Cell Ranger pipeline version 6.1.2 was used for processing the scRNA-seq datasets. Single cell gene counts for each sample were generated using *cellranger count* and mouse genome version mm10 annotated with mouse GENCODE version M28⁵⁶. There were 8,522 cells obtained for *Siah* WT (128 thousand mean reads per cell, 2674 median genes detected per cell) and 6,479 cells for *Siah2*^{-/-} (103 thousand mean reads per cell, 2502 median genes detected per cell). The gene count matrices for *Siah* WT and *Siah2*^{-/-} were aggregated and normalized for effective sequencing depth using *cellranger aggr* applying “--normalize=mapped” parameter.

Integrated analysis of scRNA-seq datasets

Aggregated gene count matrix for *Siah* WT and *Siah2*^{-/-} scRNA-seq samples were processed using Seurat version 4.0.5⁵⁷ and R version 4.0.2. 10X Genomics Cell Ranger aggr matrix was converted to Seurat object by retaining genes expressed in minimum of 10 cells and cells expressing a minimum of 200 genes. Cells expressing <10% mitochondrial genes (to remove dead/low quality cells) and <5000 genes expressed (to remove potential doublets/multiplets) were retained. Integration of *Siah* WT and *Siah2*^{-/-} samples was performed using *sctransform* normalization method (https://satijalab.org/seurat/articles/integration_introduction.html#performing-integration-on-datasets-normalized-with-sctransform-1). 3000 variable genes were used in *SelectIntegrationFeatures* step. The two datasets were integrated using *FindIntegrationAnchors(normalization.method = "SCT")* and *IntegrateData(normalization.method = "SCT")*. PCA components were computed using *RunPCA()*. Cell Clusters were computed using *RunUMAP(dims=1:30)*, *FindNeighbors()*, and *FindClusters(resolution=0.5)* resulting in 17 cell clusters. For visualization of gene expression and differential expression analysis, default assay was set to “RNA” and gene counts normalized using *NormalizeData()*. Cluster markers were found using *FindAllMarkers()*. Differential expression analysis comparisons were performed using *FindMarkers(test.use = “MAST”)*. Plots were prepared using Seurat and ggplot2. Pathway analyses were performed in Ingenuity Pathway Analysis (Qiagen, Redwood City, USA). RNA-seq and scRNA-seq main and supplemental plots were prepared using ggplot2 (H. Wickham. ggplot2: Elegant Graphics for Data Analysis. Springer-Verlag New York, 2016), ComplexHeatmap⁵⁸, and Seurat.

LUAD analysis

Gene expression (RNA-seq) and clinical data from TCGA-LUAD Pan-Cancer 2018⁵⁹ were downloaded from cBioPortal⁶⁰. Survival analysis was performed in R version 4.2.1 using survival (Therneau T (2020). A Package

for Survival Analysis in R. R package version 3.3-1, URL: <https://CRAN.R-project.org/package=survival>.), survminer (Alboukadel Kassambara, Marcin Kosinski and Przemyslaw Biecek (2020). survminer: Drawing Survival Curves using 'ggplot2'. R package version 0.4.9. <http://www.sthda.com/english/rpkgs/survminer/>), and maxstat (Torsten Hothorn (2017). Maxstat: Maximally Selected Rank Statistics. R package version 0.7-25. <https://CRAN.R-project.org/package=maxstat>) packages. Categorization of TCGA-LUAD samples as 'high' and 'low' gene expressors in TCGA data was determined using `surv_cutpoint()` and `surv_categorize()` functions from survminer package. Survival analyses using gene signatures (multiple genes) were performed by computing mean expression of the gene signature. Hazard ratios in TCGA-LUAD for each gene were computed in R with `coxph()` function using the same 'high' and 'low' gene expression categorizations described above. Wang et al. developed CODEFACS (COntident DEconvolution For All Cell Subsets), a tool deconvolving cell-type-specific gene expression in each sample from bulk expression given either precomputed estimates of cell abundance or cell-type-specific signature⁴⁴. To deconvolve TCGA-LUAD and TCGA-SCC, they first estimated abundance of 11 cell types (macrophages/dendritic cells--CD14+, B cells--CD19+, CD4+T cells, CD8+ T cells, T regulatory cells, NK cells--CD56+, endothelial cells, fibroblasts, neutrophils, basophils, eosinophils and tissue-specific tumor cells) based on bulk methylation and then applied CODEFACS to the corresponding bulk gene expression. The output is cell-type-specific gene expression profile for each sample in TCGA-LUAD and TCGA-SCC.

Statistical Analysis

GraphPad Prism version 7 was used for statistical analysis. Differences between two groups were assessed using two-tailed unpaired *t* test. Differentially expressed genes were identified in bulk RNA-seq using Wald test implemented in DESeq2. Differentially expressed genes in scRNA-seq clusters were identified using *FindMarkers()* and *MAST* test in Seurat. Survival analysis and hazard ratio p-values were computed using log-rank test. Differences in cell type compositions of TCGA-LUAD patients were tested using Wilcoxon rank sum test.

References

1. Jin MZ, Jin WL. The updated landscape of tumor microenvironment and drug repurposing. *Signal Transduct Target Ther.* 2020;5(1):166. Epub 20200825. doi: 10.1038/s41392-020-00280-x. PubMed PMID: 32843638; PMCID: PMC7447642.
2. Bejarano L, Jordao MJC, Joyce JA. Therapeutic Targeting of the Tumor Microenvironment. *Cancer Discov.* 2021;11(4):933-59. doi: 10.1158/2159-8290.CD-20-1808. PubMed PMID: 33811125.
3. van der Leun AM, Thommen DS, Schumacher TN. CD8(+) T cell states in human cancer: insights from single-cell analysis. *Nat Rev Cancer.* 2020;20(4):218-32. Epub 20200205. doi: 10.1038/s41568-019-0235-4. PubMed PMID: 32024970; PMCID: PMC7115982.
4. Murphy TL, Murphy KM. Dendritic cells in cancer immunology. *Cell Mol Immunol.* 2022;19(1):3-13. Epub 20210903. doi: 10.1038/s41423-021-00741-5. PubMed PMID: 34480145; PMCID: PMC8752832.
5. Kalluri R. The biology and function of fibroblasts in cancer. *Nat Rev Cancer.* 2016;16(9):582-98. doi: 10.1038/nrc.2016.73. PubMed PMID: 27550820.
6. Amersfoort J, Eelen G, Carmeliet P. Immunomodulation by endothelial cells - partnering up with the immune system? *Nat Rev Immunol.* 2022;22(9):576-88. Epub 20220314. doi: 10.1038/s41577-022-00694-4. PubMed PMID: 35288707; PMCID: PMC8920067.
7. Wu K, Lin K, Li X, Yuan X, Xu P, Ni P, Xu D. Redefining Tumor-Associated Macrophage Subpopulations and Functions in the Tumor Microenvironment. *Front Immunol.* 2020;11:1731. Epub 20200804. doi: 10.3389/fimmu.2020.01731. PubMed PMID: 32849616; PMCID: PMC7417513.
8. Pan Y, Yu Y, Wang X, Zhang T. Tumor-Associated Macrophages in Tumor Immunity. *Front Immunol.* 2020;11:583084. Epub 20201203. doi: 10.3389/fimmu.2020.583084. PubMed PMID: 33365025; PMCID: PMC7751482.
9. Sher T, Dy GK, Adjei AA. Small cell lung cancer. *Mayo Clin Proc.* 2008;83(3):355-67. doi: 10.4065/83.3.355. PubMed PMID: 18316005.
10. Sozio F, Schioppa T, Sozzani S, Del Prete A. Urethane-induced lung carcinogenesis. *Methods Cell Biol.* 2021;163:45-57. Epub 20201023. doi: 10.1016/bs.mcb.2020.09.005. PubMed PMID: 33785168.
11. Hwang I, Kim JW, Ylaya K, Chung EJ, Kitano H, Perry C, Hanaoka J, Fukuoka J, Chung JY, Hewitt SM. Tumor-associated macrophage, angiogenesis and lymphangiogenesis markers predict prognosis of non-small cell lung cancer patients. *J Transl Med.* 2020;18(1):443. Epub 20201123. doi: 10.1186/s12967-020-02618-z. PubMed PMID: 33228719; PMCID: PMC7686699.
12. Sedighzadeh SS, Khoshbin AP, Razi S, Keshavarz-Fathi M, Rezaei N. A narrative review of tumor-associated macrophages in lung cancer: regulation of macrophage polarization and therapeutic implications. *Transl Lung Cancer Res.* 2021;10(4):1889-916. doi: 10.21037/tlcr-20-1241. PubMed PMID: 34012800; PMCID: PMC8107755.

13. Melo EM, Oliveira VLS, Boff D, Galvao I. Pulmonary macrophages and their different roles in health and disease. *Int J Biochem Cell Biol.* 2021;141:106095. Epub 20211013. doi: 10.1016/j.biocel.2021.106095. PubMed PMID: 34653619.
14. Hou F, Xiao K, Tang L, Xie L. Diversity of Macrophages in Lung Homeostasis and Diseases. *Front Immunol.* 2021;12:753940. Epub 20210924. doi: 10.3389/fimmu.2021.753940. PubMed PMID: 34630433; PMCID: PMC8500393.
15. Tan SY, Krasnow MA. Developmental origin of lung macrophage diversity. *Development.* 2016;143(8):1318-27. Epub 20160307. doi: 10.1242/dev.129122. PubMed PMID: 26952982; PMCID: PMC4852511.
16. Schneider C, Nobs SP, Kurrer M, Rehrauer H, Thiele C, Kopf M. Induction of the nuclear receptor PPAR-gamma by the cytokine GM-CSF is critical for the differentiation of fetal monocytes into alveolar macrophages. *Nat Immunol.* 2014;15(11):1026-37. Epub 20140928. doi: 10.1038/ni.3005. PubMed PMID: 25263125.
17. Mass E, Ballesteros I, Farlik M, Halbritter F, Gunther P, Crozet L, Jacome-Galarza CE, Handler K, Klughammer J, Kobayashi Y, Gomez-Perdiguerro E, Schultze JL, Beyer M, Bock C, Geissmann F. Specification of tissue-resident macrophages during organogenesis. *Science.* 2016;353(6304). Epub 20160804. doi: 10.1126/science.aaf4238. PubMed PMID: 27492475; PMCID: PMC5066309.
18. Guilliams M, De Kleer I, Henri S, Post S, Vanhoutte L, De Prijck S, Deswarte K, Malissen B, Hammad H, Lambrecht BN. Alveolar macrophages develop from fetal monocytes that differentiate into long-lived cells in the first week of life via GM-CSF. *J Exp Med.* 2013;210(10):1977-92. Epub 20130916. doi: 10.1084/jem.20131199. PubMed PMID: 24043763; PMCID: PMC3782041.
19. Hussell T, Bell TJ. Alveolar macrophages: plasticity in a tissue-specific context. *Nat Rev Immunol.* 2014;14(2):81-93. Epub 20140121. doi: 10.1038/nri3600. PubMed PMID: 24445666.
20. Kulikauskaite J, Wack A. Teaching Old Dogs New Tricks? The Plasticity of Lung Alveolar Macrophage Subsets. *Trends Immunol.* 2020;41(10):864-77. Epub 20200904. doi: 10.1016/j.it.2020.08.008. PubMed PMID: 32896485; PMCID: PMC7472979.
21. Dehle FC, Mukaro VR, Jurisevic C, Moffat D, Ahern J, Hodge G, Jersmann H, Reynolds PN, Hodge S. Defective lung macrophage function in lung cancer +/- chronic obstructive pulmonary disease (COPD/emphysema)-mediated by cancer cell production of PGE2? *PLoS One.* 2013;8(4):e61573. Epub 20130426. doi: 10.1371/journal.pone.0061573. PubMed PMID: 23637858; PMCID: PMC3637201.
22. Scortegagna M, Hockemeyer K, Dolgalev I, Pozniak J, Rambow F, Li Y, Feng Y, Tinoco R, Otero DC, Zhang T, Brown K, Bosenberg M, Bradley LM, Marine JC, Aifantis I, Ronai ZA. Siah2 control of T-regulatory cells limits anti-tumor immunity. *Nat Commun.* 2020;11(1):99. Epub 20200107. doi: 10.1038/s41467-019-13826-7. PubMed PMID: 31911617; PMCID: PMC6946684.
23. Misharin AV, Morales-Nebreda L, Reyfman PA, Cuda CM, Walter JM, McQuattie-Pimentel AC, Chen CI, Anekalla KR, Joshi N, Williams KJN, Abdala-Valencia H, Yacoub TJ, Chi M, Chiu S, Gonzalez-Gonzalez FJ, Gates K, Lam AP, Nicholson TT, Homan PJ, Soberanes S, Dominguez S, Morgan VK, Saber R, Shaffer A,

Hinchcliff M, Marshall SA, Bharat A, Berdnikovs S, Bhorade SM, Bartom ET, Morimoto RI, Balch WE, Sznajder JI, Chandel NS, Mutlu GM, Jain M, Gottardi CJ, Singer BD, Ridge KM, Bagheri N, Shilatifard A, Budinger GRS, Perlman H. Monocyte-derived alveolar macrophages drive lung fibrosis and persist in the lung over the life span. *J Exp Med*. 2017;214(8):2387-404. Epub 20170710. doi: 10.1084/jem.20162152. PubMed PMID: 28694385; PMCID: PMC5551573.

24. Li F, Piattini F, Pohlmeier L, Feng Q, Rehrauer H, Kopf M. Monocyte-derived alveolar macrophages autonomously determine severe outcome of respiratory viral infection. *Sci Immunol*. 2022;7(73):eabj5761. Epub 20220701. doi: 10.1126/sciimmunol.abj5761. PubMed PMID: 35776802.

25. Bellezza I, Giambanco I, Minelli A, Donato R. Nrf2-Keap1 signaling in oxidative and reductive stress. *Biochim Biophys Acta Mol Cell Res*. 2018;1865(5):721-33. Epub 20180227. doi: 10.1016/j.bbamcr.2018.02.010. PubMed PMID: 29499228.

26. Baird L, Yamamoto M. The Molecular Mechanisms Regulating the KEAP1-NRF2 Pathway. *Mol Cell Biol*. 2020;40(13). Epub 20200615. doi: 10.1128/MCB.00099-20. PubMed PMID: 32284348; PMCID: PMC7296212.

27. Itoh K, Wakabayashi N, Katoh Y, Ishii T, Igarashi K, Engel JD, Yamamoto M. Keap1 represses nuclear activation of antioxidant responsive elements by Nrf2 through binding to the amino-terminal Neh2 domain. *Genes Dev*. 1999;13(1):76-86. doi: 10.1101/gad.13.1.76. PubMed PMID: 9887101; PMCID: PMC316370.

28. Sajja RK, Green KN, Cucullo L. Altered Nrf2 signaling mediates hypoglycemia-induced blood-brain barrier endothelial dysfunction in vitro. *PLoS One*. 2015;10(3):e0122358. Epub 20150325. doi: 10.1371/journal.pone.0122358. PubMed PMID: 25807533; PMCID: PMC4373930.

29. Baba K, Morimoto H, Imaoka S. Seven in absentia homolog 2 (Siah2) protein is a regulator of NF-E2-related factor 2 (Nrf2). *J Biol Chem*. 2013;288(25):18393-405. Epub 20130503. doi: 10.1074/jbc.M112.438762. PubMed PMID: 23645672; PMCID: PMC3689981.

30. Matsuzawa SI, Reed JC. Siah-1, SIP, and Ebi collaborate in a novel pathway for beta-catenin degradation linked to p53 responses. *Mol Cell*. 2001;7(5):915-26. doi: 10.1016/s1097-2765(01)00242-8. PubMed PMID: 11389839.

31. Liu J, Stevens J, Rote CA, Yost HJ, Hu Y, Neufeld KL, White RL, Matsunami N. Siah-1 mediates a novel beta-catenin degradation pathway linking p53 to the adenomatous polyposis coli protein. *Mol Cell*. 2001;7(5):927-36. doi: 10.1016/s1097-2765(01)00241-6. PubMed PMID: 11389840.

32. Jang KL, Shackelford J, Seo SY, Pagano JS. Up-regulation of beta-catenin by a viral oncogene correlates with inhibition of the seven in absentia homolog 1 in B lymphoma cells. *Proc Natl Acad Sci U S A*. 2005;102(51):18431-6. Epub 20051212. doi: 10.1073/pnas.0504054102. PubMed PMID: 16344472; PMCID: PMC1317901.

33. Sennello JA, Misharin AV, Flozak AS, Berdnikovs S, Cheres P, Varga J, Kamp DW, Budinger GR, Gottardi CJ, Lam AP. Lrp5/beta-Catenin Signaling Controls Lung Macrophage Differentiation and Inhibits

Resolution of Fibrosis. *Am J Respir Cell Mol Biol*. 2017;56(2):191-201. doi: 10.1165/rcmb.2016-0147OC. PubMed PMID: 27668462; PMCID: PMC5359648.

34. Huang R, Wang S, Wang N, Zheng Y, Zhou J, Yang B, Wang X, Zhang J, Guo L, Wang S, Chen Z, Wang Z, Xiang S. CCL5 derived from tumor-associated macrophages promotes prostate cancer stem cells and metastasis via activating beta-catenin/STAT3 signaling. *Cell Death Dis*. 2020;11(4):234. Epub 20200416. doi: 10.1038/s41419-020-2435-y. PubMed PMID: 32300100; PMCID: PMC7162982.

35. Feng Y, Ren J, Gui Y, Wei W, Shu B, Lu Q, Xue X, Sun X, He W, Yang J, Dai C. Wnt/beta-Catenin-Promoted Macrophage Alternative Activation Contributes to Kidney Fibrosis. *J Am Soc Nephrol*. 2018;29(1):182-93. Epub 20171011. doi: 10.1681/ASN.2017040391. PubMed PMID: 29021383; PMCID: PMC5748914.

36. Weinstock A, Rahman K, Yaacov O, Nishi H, Menon P, Nikain CA, Garabedian ML, Pena S, Akbar N, Sansbury BE, Heffron SP, Liu J, Marecki G, Fernandez D, Brown EJ, Ruggles KV, Ramsey SA, Giannarelli C, Spite M, Choudhury RP, Loke P, Fisher EA. Wnt signaling enhances macrophage responses to IL-4 and promotes resolution of atherosclerosis. *Elife*. 2021;10. Epub 20210315. doi: 10.7554/eLife.67932. PubMed PMID: 33720008; PMCID: PMC7994001.

37. Liu L, Carron B, Yee HT, Yie TA, Hajjou M, Rom W. Wnt pathway in pulmonary fibrosis in the bleomycin mouse model. *J Environ Pathol Toxicol Oncol*. 2009;28(2):99-108. doi: 10.1615/jenviropatholtoxiconcol.v28.i2.20. PubMed PMID: 19817697; PMCID: PMC3704199.

38. Gurley KE, Moser RD, Kemp CJ. Induction of Lung Tumors in Mice with Urethane. *Cold Spring Harb Protoc*. 2015;2015(9):pdb prot077446. Epub 20150901. doi: 10.1101/pdb.prot077446. PubMed PMID: 26330618.

39. Xie N, Cui H, Ge J, Banerjee S, Guo S, Dubey S, Abraham E, Liu RM, Liu G. Metabolic characterization and RNA profiling reveal glycolytic dependence of profibrotic phenotype of alveolar macrophages in lung fibrosis. *Am J Physiol Lung Cell Mol Physiol*. 2017;313(5):L834-L44. Epub 20170810. doi: 10.1152/ajplung.00235.2017. PubMed PMID: 28798256; PMCID: PMC5792180.

40. Chun SH, Cha YN, Kim C. Urethane increases reactive oxygen species and activates extracellular signal-regulated kinase in RAW 264.7 macrophages and A549 lung epithelial cells. *Arch Pharm Res*. 2013;36(6):775-82. Epub 20130401. doi: 10.1007/s12272-013-0104-8. PubMed PMID: 23543651.

41. Bauer AK, Cho HY, Miller-Degraff L, Walker C, Helms K, Fostel J, Yamamoto M, Kleeberger SR. Targeted deletion of Nrf2 reduces urethane-induced lung tumor development in mice. *PLoS One*. 2011;6(10):e26590. Epub 20111021. doi: 10.1371/journal.pone.0026590. PubMed PMID: 22039513; PMCID: PMC3198791.

42. Aran D, Looney AP, Liu L, Wu E, Fong V, Hsu A, Chak S, Naikawadi RP, Wolters PJ, Abate AR, Butte AJ, Bhattacharya M. Reference-based analysis of lung single-cell sequencing reveals a transitional profibrotic macrophage. *Nat Immunol*. 2019;20(2):163-72. Epub 20190114. doi: 10.1038/s41590-018-0276-y. PubMed PMID: 30643263; PMCID: PMC6340744.

43. Reyfman PA, Walter JM, Joshi N, Anekalla KR, McQuattie-Pimentel AC, Chiu S, Fernandez R, Akbarpour M, Chen CI, Ren Z, Verma R, Abdala-Valencia H, Nam K, Chi M, Han S, Gonzalez-Gonzalez FJ, Soberanes S, Watanabe S, Williams KJN, Flozak AS, Nicholson TT, Morgan VK, Winter DR, Hinchcliff M, Hrusch CL, Guzy RD, Bonham CA, Sperling AI, Bag R, Hamanaka RB, Mutlu GM, Yeldandi AV, Marshall SA, Shilatifard A, Amaral LAN, Perlman H, Sznajder JI, Argento AC, Gillespie CT, Dematte J, Jain M, Singer BD, Ridge KM, Lam AP, Bharat A, Bhorade SM, Gottardi CJ, Budinger GRS, Misharin AV. Single-Cell Transcriptomic Analysis of Human Lung Provides Insights into the Pathobiology of Pulmonary Fibrosis. *Am J Respir Crit Care Med*. 2019;199(12):1517-36. doi: 10.1164/rccm.201712-2410OC. PubMed PMID: 30554520; PMCID: PMC6580683.
44. Wang K, Patkar S, Lee JS, Gertz EM, Robinson W, Schischlik F, Crawford DR, Schaffer AA, Ruppin E. Deconvolving Clinically Relevant Cellular Immune Cross-talk from Bulk Gene Expression Using CODEFACS and LIRICS Stratifies Patients with Melanoma to Anti-PD-1 Therapy. *Cancer Discov*. 2022;12(4):1088-105. doi: 10.1158/2159-8290.CD-21-0887. PubMed PMID: 34983745; PMCID: PMC8983586.
45. Yu X, Buttgereit A, Lelios I, Utz SG, Cansever D, Becher B, Greter M. The Cytokine TGF-beta Promotes the Development and Homeostasis of Alveolar Macrophages. *Immunity*. 2017;47(5):903-12 e4. Epub 20171107. doi: 10.1016/j.immuni.2017.10.007. PubMed PMID: 29126797.
46. Zhou HC, Xin-Yan Y, Yu WW, Liang XQ, Du XY, Liu ZC, Long JP, Zhao GH, Liu HB. Lactic acid in macrophage polarization: The significant role in inflammation and cancer. *Int Rev Immunol*. 2022;41(1):4-18. Epub 20210725. doi: 10.1080/08830185.2021.1955876. PubMed PMID: 34304685.
47. Colegio OR. Lactic acid polarizes macrophages to a tumor-promoting state. *Oncoimmunology*. 2016;5(3):e1014774. Epub 20150319. doi: 10.1080/2162402X.2015.1014774. PubMed PMID: 27141329; PMCID: PMC4839384.
48. Afik R, Zigmond E, Vugman M, Klepfish M, Shimshoni E, Pasmanik-Chor M, Shenoy A, Bassat E, Halpern Z, Geiger T, Sagi I, Varol C. Tumor macrophages are pivotal constructors of tumor collagenous matrix. *J Exp Med*. 2016;213(11):2315-31. Epub 20161003. doi: 10.1084/jem.20151193. PubMed PMID: 27697834; PMCID: PMC5068227.
49. Deligne C, Midwood KS. Macrophages and Extracellular Matrix in Breast Cancer: Partners in Crime or Protective Allies? *Front Oncol*. 2021;11:620773. Epub 20210224. doi: 10.3389/fonc.2021.620773. PubMed PMID: 33718177; PMCID: PMC7943718.
50. Nayak DK, Mendez O, Bowen S, Mohanakumar T. Isolation and In Vitro Culture of Murine and Human Alveolar Macrophages. *J Vis Exp*. 2018(134). Epub 20180420. doi: 10.3791/57287. PubMed PMID: 29733312; PMCID: PMC6100701.
51. Martin M. Cutadapt removes adapter sequences from high-throughput sequencing reads. *EMBnetjournal*. 2011;v. 17(ISSN 2226-6089):pp. 10-2
52. Dobin A, Davis CA, Schlesinger F, Drenkow J, Zaleski C, Jha S, Batut P, Chaisson M, Gingeras TR. STAR: ultrafast universal RNA-seq aligner. *Bioinformatics*. 2013;29(1):15-21. Epub 20121025. doi: 10.1093/bioinformatics/bts635. PubMed PMID: 23104886; PMCID: PMC3530905.

53. Li B, Dewey CN. RSEM: accurate transcript quantification from RNA-Seq data with or without a reference genome. *BMC Bioinformatics*. 2011;12:323. Epub 20110804. doi: 10.1186/1471-2105-12-323. PubMed PMID: 21816040; PMCID: PMC3163565.
54. Ewels P, Magnusson M, Lundin S, Kaller M. MultiQC: summarize analysis results for multiple tools and samples in a single report. *Bioinformatics*. 2016;32(19):3047-8. Epub 20160616. doi: 10.1093/bioinformatics/btw354. PubMed PMID: 27312411; PMCID: PMC5039924.
55. Love MI, Huber W, Anders S. Moderated estimation of fold change and dispersion for RNA-seq data with DESeq2. *Genome Biol*. 2014;15(12):550. doi: 10.1186/s13059-014-0550-8. PubMed PMID: 25516281; PMCID: PMC4302049.
56. Frankish A, Diekhans M, Jungreis I, Lagarde J, Loveland JE, Mudge JM, Sisu C, Wright JC, Armstrong J, Barnes I, Berry A, Bignell A, Boix C, Carbonell Sala S, Cunningham F, Di Domenico T, Donaldson S, Fiddes IT, Garcia Giron C, Gonzalez JM, Grego T, Hardy M, Hourlier T, Howe KL, Hunt T, Izuogu OG, Johnson R, Martin FJ, Martinez L, Mohanan S, Muir P, Navarro FCP, Parker A, Pei B, Pozo F, Riera FC, Ruffier M, Schmitt BM, Stapleton E, Suner MM, Sycheva I, Uszczynska-Ratajczak B, Wolf MY, Xu J, Yang YT, Yates A, Zerbino D, Zhang Y, Choudhary JS, Gerstein M, Guigo R, Hubbard TJP, Kellis M, Paten B, Tress ML, Flicek P. *Genome* 2021. *Nucleic Acids Res*. 2021;49(D1):D916-D23. doi: 10.1093/nar/gkaa1087. PubMed PMID: 33270111; PMCID: PMC7778937.
57. Stuart T, Butler A, Hoffman P, Hafemeister C, Papalexi E, Mauck WM, 3rd, Hao Y, Stoeckius M, Smibert P, Satija R. Comprehensive Integration of Single-Cell Data. *Cell*. 2019;177(7):1888-902 e21. Epub 20190606. doi: 10.1016/j.cell.2019.05.031. PubMed PMID: 31178118; PMCID: PMC6687398.
58. Gu Z, Eils R, Schlesner M. Complex heatmaps reveal patterns and correlations in multidimensional genomic data. *Bioinformatics*. 2016;32(18):2847-9. Epub 20160520. doi: 10.1093/bioinformatics/btw313. PubMed PMID: 27207943.
59. Hoadley KA, Yau C, Hinoue T, Wolf DM, Lazar AJ, Drill E, Shen R, Taylor AM, Cherniack AD, Thorsson V, Akbani R, Bowlby R, Wong CK, Wiznerowicz M, Sanchez-Vega F, Robertson AG, Schneider BG, Lawrence MS, Noushmehr H, Malta TM, Cancer Genome Atlas N, Stuart JM, Benz CC, Laird PW. Cell-of-Origin Patterns Dominate the Molecular Classification of 10,000 Tumors from 33 Types of Cancer. *Cell*. 2018;173(2):291-304 e6. doi: 10.1016/j.cell.2018.03.022. PubMed PMID: 29625048; PMCID: PMC5957518.
60. Cerami E, Gao J, Dogrusoz U, Gross BE, Sumer SO, Aksoy BA, Jacobsen A, Byrne CJ, Heuer ML, Larsson E, Antipin Y, Reva B, Goldberg AP, Sander C, Schultz N. The cBio cancer genomics portal: an open platform for exploring multidimensional cancer genomics data. *Cancer Discov*. 2012;2(5):401-4. doi: 10.1158/2159-8290.CD-12-0095. PubMed PMID: 22588877; PMCID: PMC3956037.

Figure legends

Figure 1. Siah1a and Siah2 are required for AM terminal differentiation and maturation. **A-C** Quantification of CD11b⁺ F480⁺ (A) and CD11b low F480⁺ (B) immune cells, and AMs (CD11b low F480⁺ CD11c⁺ SiglecF⁺) (C) from lungs of *WT* and *cSiah1a/2^{ff}::Lyz2^{Cre}* mice at homeostatic state. Quantification is shown as a percentage of indicated immune cells among CD45.2⁺ cells. n=7 for both genotypes. **D, E** Quantification of AMs positive for SiglecF and CD11c (D) or CD11c⁺ and SiglecF low (E) from lungs of *WT* and *cSiah1a/2^{ff}::Lyz2^{Cre}* mice. Quantification is shown as a frequency of immune cells among CD11b low F480⁺ cells. n=7 for both genotypes. **F** FACS analysis of expression of CD11c⁺ SiglecF⁺ cells by a gated subpopulation (CD11b low F480⁺ cells) of CD45.2⁺ cells from *WT* and *cSiah1a/2^{ff}::Lyz2^{Cre}* lungs. **G** Expression of CD11b, CD11c and SiglecF on AMs (CD11b low F480⁺ CD11c⁺ SiglecF⁺ cells) based on flow cytometry analysis of lungs from *WT* and *cSiah1a/2^{ff}::Lyz2^{Cre}* mice. n=7 for both genotypes. **H** CD11c⁺ and CD11c⁻ cell frequency within the population of *WT* and *cSiah1a/2^{ff}::Lyz2^{Cre}* IMs (CD11b⁺ F480⁺). n=7 for both genotypes. **I, J** Quantification of AMs and CD11c⁺ and CD11c⁻ IMs from lungs of *WT* and *cSiah1a^{ff}::Lyz2^{Cre}* (I) and *cSiah2^{ff}::Lyz2^{Cre}* (J) mice at a homeostatic state. Shown is a percentage of indicated immune cells among CD45.2⁺ cells. n=6 for *WT*; n=5 for *cSiah1a^{ff}::Lyz2^{Cre}*; n=6 for *WT*; n=5 for *cSiah2^{ff}::Lyz2^{Cre}*. **K** Quantification of AMs and CD11c⁺ and CD11c⁻ IMs from *WT* and *cSiah1a^{ff}::CD11c^{Cre}*, *cSiah1a/2^{ff}::CD11c^{Cre}* and *cSiah2^{ff}::CD11c^{Cre}* mice. Quantification is shown as a percentage of indicated immune cells among CD45.2⁺ cells. n=7 for *WT*; n=5 for *cSiah1a^{ff}::CD11c^{Cre}*; n=8 for *cSiah2^{ff}::CD11c^{Cre}*; n=6 for *cSiah1a/2^{ff}::CD11c^{Cre}*. **L** CD11c, CD206, and SiglecF expression on AMs (CD11b low F480⁺ CD11c⁺ SiglecF⁺ cells), based on flow cytometry analysis of lungs from *WT* and *cSiah1a^{ff}::CD11c^{Cre}*, *cSiah2^{ff}::CD11c^{Cre}* and *cSiah1a/2^{ff}::CD11c^{Cre}* mice. n=7 for *WT*; n=5 for *cSiah1a^{ff}::CD11c^{Cre}*; n=8 for *cSiah2^{ff}::CD11c^{Cre}*; n=6 for *cSiah1a/2^{ff}::CD11c^{Cre}*. **M** Representative flow cytometry showing expression of CD11c⁺ SiglecF⁺ cells by a gated subpopulation (CD11b low F480⁺ cells) of CD45.2⁺ cells from *WT* and *cSiah1a^{ff}::CD11c^{Cre}*, *cSiah2^{ff}::CD11c^{Cre}* and *cSiah1a/2^{ff}::CD11c^{Cre}* lungs. Data were analyzed by unpaired t-test.

Figure 2. Siah1a and Siah2 regulate maturation of fetal monocytes to AMs. **A, B** Quantification of pre-alveolar macrophages showing intermediate expression of CD11c and F4/80 (A), and expression of CD11c, CD11b and F480 on Pre-AMs (B) from E17.5 lungs of *WT* and *cSiah1a/2^{ff}::Lyz2^{Cre}* embryos. Quantification is shown as the frequency of immune cells among CD45.2⁺ cells. n=9 for *WT*; n=9 for *cSiah1a/2^{ff}::Lyz2^{Cre}*. **C**, Frequency of immune cells (F480⁺ CD11b low) in CD45⁺ cells, and of CD11c⁺ SiglecF⁺ immune cells in F480⁺

CD11b low immune cells from neonatal lungs (Day 0) of *WT* (n=8) and *cSiah1a/2^{ff}::CD11c^{Cre}* pups (n=8). **D** CD11c, F480 and SiglecF expression on AMs (CD11b low F4/80⁺ SiglecF⁺ CD11c⁺) from neonatal lungs (Day 0) of *WT* (n=8) and *cSiah1a/2^{ff}::CD11c^{Cre}* pups (n=8). **E** Representative flow cytometry plots of the frequency of CD11c⁺ SiglecF⁺ cells by a gated subpopulation (CD11b low F480⁺ cells) of CD45.2⁺ cells from *WT* and *cSiah1a/2^{ff}::CD11c^{Cre}* lungs. n=8 for *WT*; n=8 for *cSiah1a/2^{ff}::Lyz2^{Cre}*. Data were analyzed by unpaired t-test.

Figure 3. AM regeneration from in bone marrow requires Siah1a and Siah2. Bone marrow cells from *cSiah1a/2^{ff}::Lyz2^{Cre}* (CD45.2⁺) or CD45.2 *WT* mice were co-transferred with competitor CD45.1 bone marrow cells into lethally-irradiated C57Bl6 mice and lungs were harvested 10 weeks later. **A, B** Flow cytometry representation (A) and quantitation (B) of CD45.2-positive cells on lung AMs (CD11b low F4/80⁺ CD11c⁺ SiglecF⁺) from irradiated mice co-transfected with either a mix (1:1) of *cSiah1a/2^{ff}::Lyz2^{Cre}* CD45.2⁺ : CD45.1⁺ cells (n=6) or CD45.2 *WT*: CD45.1⁺ cells (n=6). **C** F4/80, CD11c, and SiglecF expression on CD45.2⁺ AMs of *cSiah1a/2^{ff}::Lyz2^{Cre}* CD45.2⁺ : CD45.1⁺ or CD45.2 *WT*: CD45.1⁺ co-transfected mice. n=6 for both genotypes. **D** Flow cytometry quantitation of CD45.2-positive cells on lung CD11c⁺ IMs (CD11b⁺ F4/80⁺ CD11c⁺) from irradiated mice co-transfected with either a mix (1:1) of *cSiah1a/2^{ff}::Lyz2^{Cre}* CD45.2⁺ : CD45.1⁺ cells (n=6) or CD45.2 *WT*: CD45.1⁺ cells (n=6). **E** Flow cytometry quantitation of CD45.2-positive cells on lung CD11c⁻ IMs (CD11b⁺ F4/80⁺ CD11c⁻), monocytes (CD11b⁺ Ly6c), neutrophils (CD11b⁺ Ly6G⁺), and CD4⁺ or CD8⁺ cells from irradiated mice co-transfected with either a mix (1:1) of *cSiah1a/2^{ff}::Lyz2^{Cre}* CD45.2⁺ : CD45.1⁺ cells (n=6) or CD45.2 *WT*: CD45.1⁺ cells (n=6). Data were analyzed by unpaired t-test.

Figure 4. Siah1a and Siah2 control AM immunoregulatory function in homeostatic conditions. RNA-seq analysis of CD11c⁺ F480⁺ SiglecF⁺ cells sorted from lungs of *WT* (n=3), *cSiah1a/2^{ff}::Lyz2^{Cre}* (n=3), or *cSiah1a/2^{ff}::CD11c^{Cre}* (n=1) mice. Each sample was a pool of 3 lungs. **A** Principal component analysis (PCA) plot based on gene expression. *WT* and *KO* samples segregate along the main principal component (PC1). **B** Volcano plot of genes differentially expressed in *KO* versus *WT* lung, based on RNA-seq. Selected up- and down-regulated genes are shown. N= 3 for both genotypes. **C** Bar plots depicting the activation z-scores and significance p-values of the most upregulated pathways in *cSiah1a/2^{ff}::Lyz2^{Cre}* compared to *WT* AMs. **D** Heatmap showing row-wise z-scores of expression of selected genes associated with particular functions induced by NRF2 from *WT* and *cSiah1a/2^{ff}::Lyz2^{Cre}* AMs based on RNA-seq analysis. n = 3 for both genotypes. Samples (columns) were hierarchically clustered. **E** Primary AMs were collected after 6 days of culture for western blot analysis. *WT* and *cSiah1a/2^{ff}::Lyz2^{Cre}* AM lysates were immunoblotted for NRF2. HSP90 was used as a loading control. n = 3

for both genotypes. **F** Primary AMs were cultured 6 days for QPCR analysis of indicated transcripts. $n = 3$ for both genotypes. **G** (left) β -catenin staining of primary AMs cultured overnight in media containing GM-CSF and (right) quantification. $n = 3$ for each genotype. β -catenin = green, Dapi = blue. Scale bar, 600 μ M. **H** Primary AMs were cultured 6 days for QPCR analysis of indicated transcripts. $n = 3$ for both genotypes. **I, J** Expression of transcripts induced by β -catenin/STAT3 or following treatment with bleomycin (**I**) implicated in glycolysis (**J**) from WT and *cSiah1a/2^{ff}::Lyz2^{Cre}* AMs based on RNA-seq analysis. $n = 3$ for both genotypes. Data in panel F, G and H were analyzed by unpaired t-test, data in panel J were analyzed by Wade test.

Figure 5. Siah1a and Siah2 deletion in macrophages promotes lung cancer following urethane treatment.

Urethane (1mg/g mouse weight) was injected intraperitoneally once a week for 6 weeks and lungs were collected 22 weeks after the first injection. **A, B** Lungs were processed, and lung nodule number (**A**) and size (**B**) were quantified by H&E staining. $n=6$ for WT, $n=5$ for *cSiah1a/2^{ff}::Lyz2^{Cre}* in panel A; $n=21$ for WT, $n=44$ for *cSiah1a/2^{ff}::Lyz2^{Cre}* in panel B. **C** Representative image of H&E staining of lungs for each genotype. Scale bar, 300 μ M. **D** AM frequencies among CD45⁺ lung cells after urethane injection. $n = 8$ for each genotype. **E** Frequencies of CD11c⁺ SiglecF⁺ (mature macrophages) and CD11c⁺ SiglecF⁻, CD11c⁻ SiglecF⁻ (immature AMs) among CD11b low F4/80⁺ cells. $n = 8$ for each genotype. **F** Representative flow cytometry plots showing CD11c⁺ SiglecF⁺ expression by a gated subpopulation (CD11b low F480⁺ cells) of CD45.2⁺ cells from WT and *cSiah1a/2^{ff}::Lyz2^{Cre}* lungs. **G** Expression of CD11c, SiglecF, CD206, CD80 and MHCI on an AM (CD11b low F4/80⁺ CD11c⁺ SiglecF⁺) population. $n = 8$ for each genotype. **H, I** Frequencies of CD11c⁺ (**H**) and CD11c⁻ (**I**) IMs among CD45⁺ cells. $n = 8$ for each genotype. Data were analyzed by unpaired t-test.

Figure 6. Siah1a and Siah2 deletion in macrophages promotes an immature state and induces an immunoregulatory/pro-fibrotic phenotype in specific macrophage clusters.

CD45⁺ cells were sorted by flow cytometry from WT and *cSiah1a/2^{ff}::Lyz2^{Cre}* lungs collected 7 weeks after the first urethane injection, and single cell RNA-seq was performed. **A** UMAP plot of CD45⁺ cells from WT ($n=7884$ cells) and *cSiah1a/2^{ff}::Lyz2^{Cre}* ($n=6035$ cells) lungs showing 17 distinct clusters. Immune cell types identified using expression of specific cell markers are labeled. **B** Scaled expression levels of selected markers used to identify clusters in the UMAP of CD45⁺ cells. **C-E** Violin plots comparing expression of genes in WT and *cSiah1a/2^{ff}::Lyz2^{Cre}* cells in macrophages (cluster 2) regulated by β -catenin or modulated upon treatment with bleomycin (**C**) or functioning in glycolysis (**D**) or macrophage differentiation (**E**). **F** Violin plots comparing expression of genes in monocytes

(cluster 3) regulated by β -catenin or modulated by bleomycin treatment. Data were analyzed using *FindMarkers()* and *MAST* test in Seurat.

Figure 7. Siah1a and Siah2 deletion in macrophages promotes an immunoregulatory/pro-fibrotic phenotype in monocyte-derived AMs. Myeloid cell clusters (2, 3, and 5 from global UMAP in Figure 6A) from single cell RNA-seq analysis of CD45⁺ cells were re-clustered to obtain higher resolution clustering of myeloid cells. **A.** UMAP plot of myeloid cells from WT (n=2245 cells) and *cSiah1a/2^{ff}::Lyz2^{Cre}* (n=1417 cells) lungs showing 9 distinct clusters. **B.** Heat map of expression levels of markers of monocytic origin in each myeloid cell cluster. **C.** Dot plots showing scaled expression of marker genes used to identify specific sub-clusters of myeloid cells. **D, E.** Violin plots comparing expression of genes from sub-cluster 0 functioning in AM differentiation (D) or regulated by β -catenin or following bleomycin treatment (E) in each genotype. **F** Average expression of 65 out of 72 upregulated genes in sub-cluster 0 (KO vs. WT) found in TCGA- LUAD RNA-seq dataset was used to stratify patients as high (n=65) and low (n=436) expressors of this 65-gene signature. Patients with high expression of the gene signature show worse overall survival (p-value=2.97e-07, log rank test) compared to low expressors. **G** Cell type compositions of TCGA-LUAD patient tumors were assessed using cell-type and gene-expression deconvolution dataset from CODEFACS. The same patient stratifications as Figure 7F were used. Shown are comparisons of 10 cell type composition fractions of high and low expressors of the inflammatory gene signature in sub-cluster 0. P-values for composition difference in each type cell type are shown (Wilcoxon rank sum test). Data in panels D and E were analyzed using *FindMarkers()* and *MAST* test in Seurat.

Supplemental Figures

Sup. Figure 1. Siah1a/2-deleted macrophages exhibit a specific immune phenotype in lung tissue. **A** Frequency of F480⁺ CD11b⁺ immune cells among CD45⁺ cells from kidney, spleen and heart. n=8 for WT; n=7 for *Siah1a^{ff} : Siah2^{ff} : Lyz2-Cre*. **B** Quantification of CD45⁺ cells from lungs of WT and *cSiah1a/2^{ff}::Lyz2^{Cre}* mice at a homeostatic state. Quantification is shown as a percentage of immune cells among total cells. n=7 for WT; n=7 for *cSiah1a/2^{ff}::Lyz2^{Cre}*. **C** Frequency of CD206⁺ cells among F480⁺ CD11b low cells from lung. n=7 for both genotypes. **D** Expression of F4/80, MHCI, CD80, and CD206 on AMs (CD11b low F480⁺ CD11c⁺ SiglecF⁺ cells) based on flow cytometry analysis of lungs from WT and *cSiah1a/2^{ff}::Lyz2^{Cre}* mice. n=7 for WT;

n=7 for *cSiah1a/2^{ff}::Lyz2^{Cre}*. **E** Frequency of CD206⁺ cells and expression of CD11c among CD11c⁺ IMs of lungs of WT and *cSiah1a/2^{ff}::Lyz2^{Cre}* mice. n=7 for both genotypes. **F** Frequency of NK1⁺, LY6C⁺ CD11b⁺, LY6G⁺ CD11b⁺, CD4⁺, CD8⁺, and B220⁺ NK1⁻ immune cells among CD45⁺ cells from lungs of WT and *cSiah1a/2^{ff}::Lyz2^{Cre}* mice. n=7 for both genotypes. **G** Frequency of CD11b⁺ and F4/80⁺ cells among CD45⁺ cells, and frequency of CD11c⁺ and CD11c⁻ among IMs of lungs of WT and *cSiah1a^{ff}::Lyz2^{Cre}* mice or *cSiah2^{ff}::Lyz2^{Cre}* mice. n=6 for WT, n = 5 for *cSiah1a^{ff}::Lyz2^{Cre}*; n = 6 for WT, n = 6 for *cSiah2^{ff}::Lyz2^{Cre}*. **H** Quantification of CD45⁺ cells of WT, *cSiah1a^{ff}::CD11c^{Cre}*, *cSiah2^{ff}::CD11c^{Cre}* and *cSiah1a/2^{ff}::CD11c^{Cre}* mice. Quantification is shown as a percentage of indicated immune cells among total cells. n=7 for WT; n=5 for *cSiah1a^{ff}::CD11c^{Cre}*; n=8 for *cSiah2^{ff}::CD11c^{Cre}*; n=6 for *cSiah1a/2^{ff}::CD11c^{Cre}*. **I** Quantification of dendritic cells (DCs), neutrophils, B cells, and CD4⁺ or CD8⁺ cells from WT, *cSiah1a^{ff}::CD11c^{Cre}*, *cSiah2^{ff}::CD11c^{Cre}* and *cSiah1a/2^{ff}::CD11c^{Cre}* mice. Quantification is shown as a percentage of indicated immune cells among CD45.2⁺ cells. n=7 for WT; n=5 for *cSiah1a^{ff}::CD11c^{Cre}*; n=8 for *cSiah2^{ff}::CD11c^{Cre}* n=6 for *cSiah1a/2^{ff}::CD11c^{Cre}*. **J** Quantification of NK1⁺ cells from WT and *cSiah1a/2^{ff}::CD11c^{Cre}* mice. Quantification is shown as a percentage of indicated immune cells among CD45.2⁺ cells. n=11 for WT; n=13 for *cSiah1a/2^{ff}::CD11c^{Cre}*. Data were analyzed by unpaired t-test.

Sup. Figure 2. Frequency of selected immune cells in lungs of transplanted mice. Bone marrow cells from *cSiah1a/2^{ff}::CD11c^{Cre}* (CD45.2⁺) or CD45.2 WT mice were co-transferred with CD45.1 competitors bone marrow cells into lethally-irradiated C57Bl6 mice, and lungs were harvested 10 weeks later. **A** Flow cytometry quantitation of CD45.2 positive cells on lung AMs (CD11b low F4/80⁺ CD11c⁺ SiglecF⁺) from irradiated mice co-transfected with either a mix (1:1) of *cSiah1a/2^{ff}::CD11c^{Cre}* CD45.2⁺ : CD45.1⁺ cells (n=6) or CD45.2 WT: CD45.1⁺ cells (n=6). **B** CD11c expression on CD45.2⁺ AMs of *cSiah1a/2^{ff}::CD11c^{Cre}* CD45.2⁺ : CD45.1⁺ or CD45.2 WT: CD45.1⁺ co-transfected mice. n=6 for both genotypes. **C** Flow cytometry quantitation of CD45.2⁺ positive cells on lung CD11c⁺ and CD11c⁻ IMs (CD11b⁺ F4/80⁺ CD11c⁻) from irradiated mice co-transfected with either a mix (1:1) of *cSiah1a/2^{ff}::CD11c^{Cre}* CD45.2⁺ : CD45.1⁺ cells (n=6) or CD45.2 WT: CD45.1⁺ cells (n=6). Data were analyzed by unpaired t-test.

Sup. Figure 3. Siah1a/2 deletion in AMs promotes β catenin nuclear localization. RNA-seq analysis of CD11c⁺ F480⁺ SiglecF⁺ cells sorted from lungs of WT (n=3), *cSiah1a/2^{ff}::Lyz2^{Cre}* (n=3), *cSiah1a/2^{ff}::CD11c^{Cre}* (n=1) mice. Each sample was a pool of 3 lungs. **A** Heatmap showing differentially expressed genes in *cSiah1a/2^{ff}::Lyz2^{Cre}* vs. WT comparison. Also shown is expression for the same genes in *cSiah1a/2^{ff}::CD11c^{Cre}*

indicating that *cSiah1a/2^{ff}::Lyz2^{Cre}* and *cSiah1a/2^{ff}::CD11c^{Cre}* AMs show similar gene expression patterns. **B** Expression levels of selected genes from WT and *Siah1a^{ff}: Siah2^{ff}: Lyz2-Cre* AMs based on RNA-seq gene expression data. n = 3 for both genotypes. **C** PPAR γ staining of primary AMs cultured overnight in media containing GM-CSF. PPAR γ = green, Dapi = blue. n = 3 for each genotype. Scale bar, 600 μ M. **D** Primary bone marrow-derived macrophages (BMDMs) were cultured 9 days for western blot analysis. Lysates from WT and *cSiah1a/2^{ff}::Lyz2^{Cre}* BMDMs were immunoblotted for NRF2. HSP90 was used as a loading control. n = 3 for both genotypes. **E** Staining for non-phosphorylated Ser45 (active) β -catenin in AMs cultured overnight in media containing GM-CSF and quantification. β -catenin = green, Dapi = blue. n = 3 for each genotype. Scale bar, 600 μ M. Data in panel B were analyzed by Wade test.

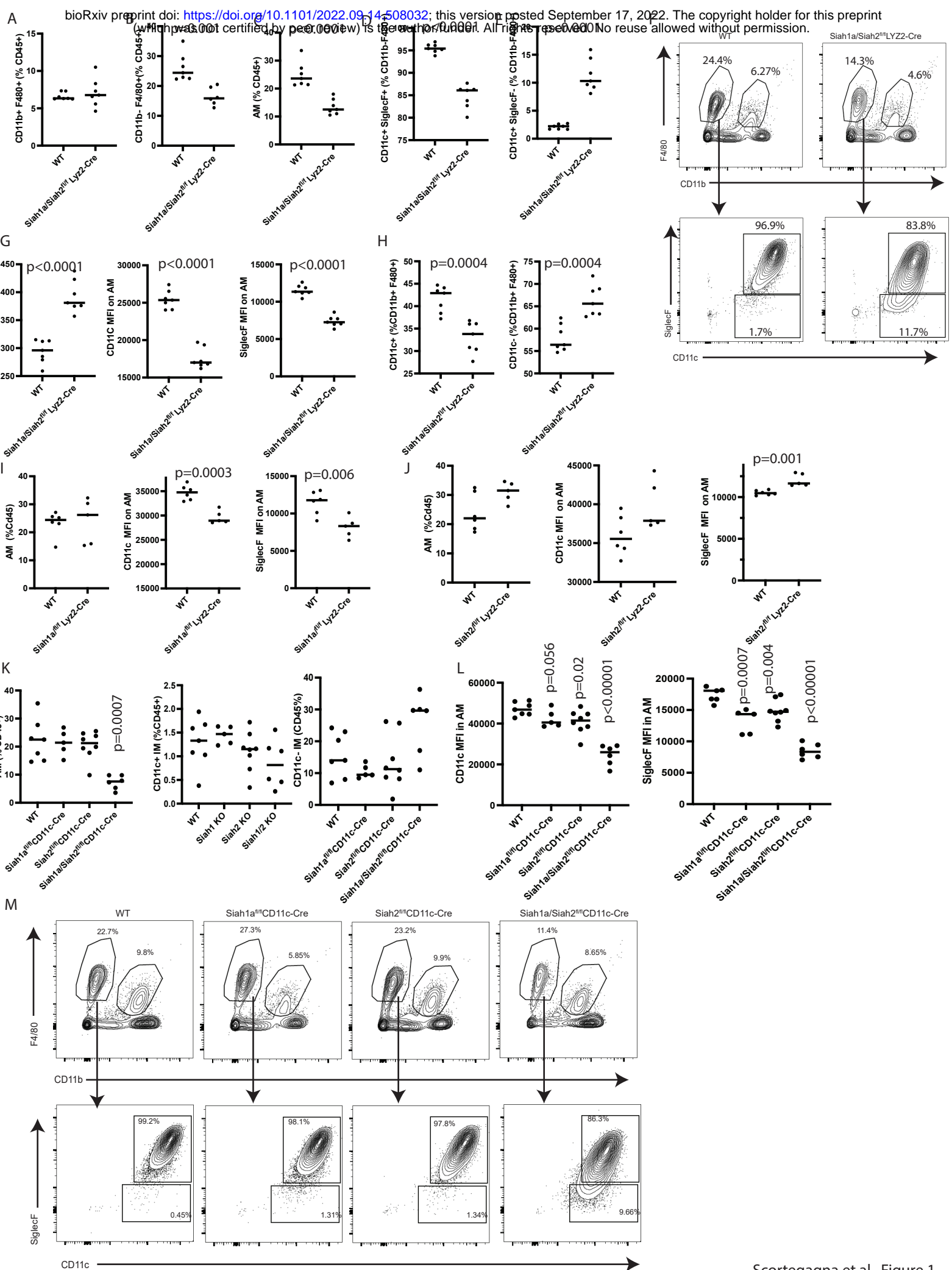
Sup. Figure 4. Siah1a/2 deletion in macrophages promotes lung cancer following urethane treatment.

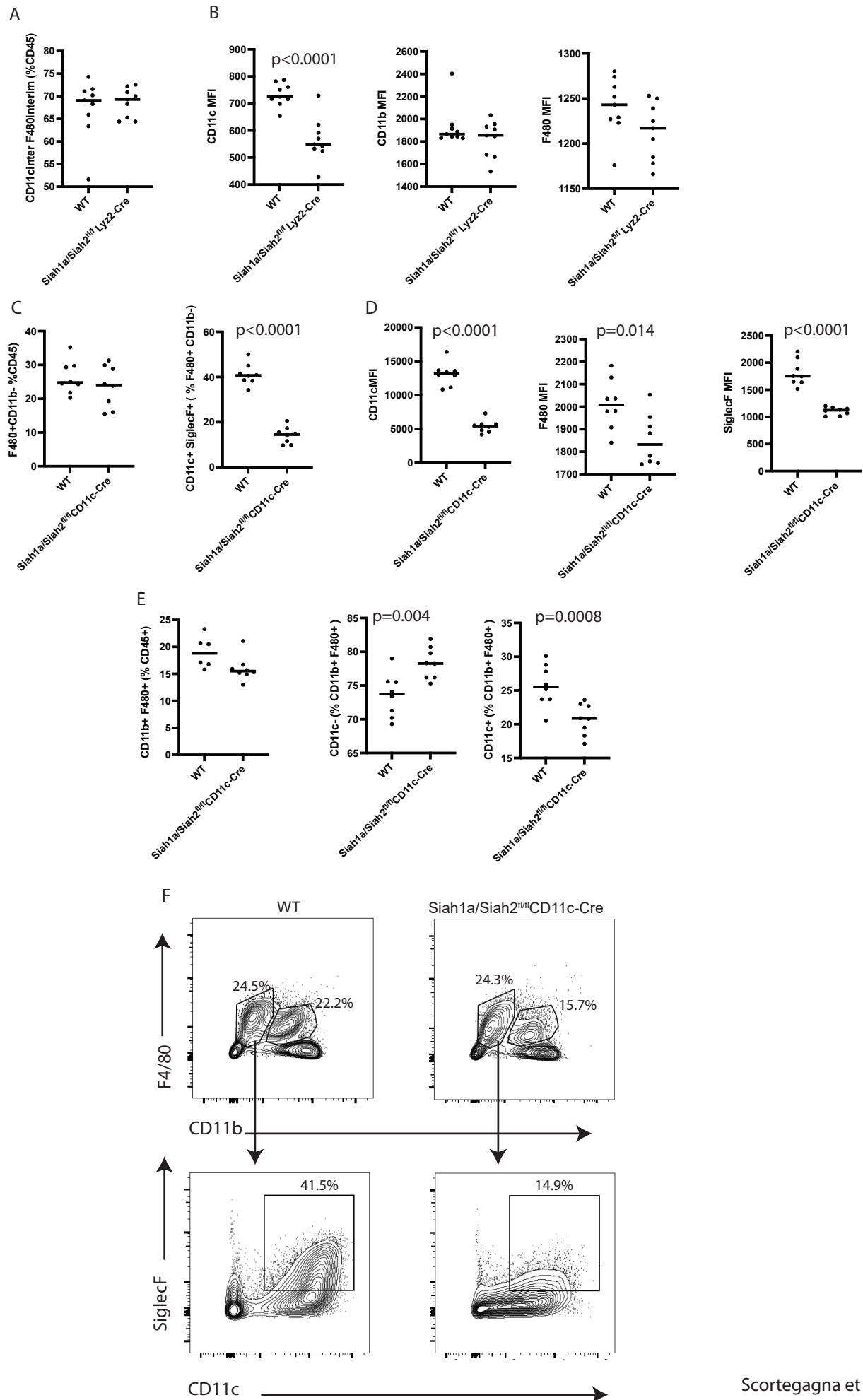
Urethane (1 mg/g of mouse weight) was injected intraperitoneally once a week for 6 weeks, and lungs were collected 22 weeks later. **A** Frequencies of CD45⁺ cells among total cells of lungs after urethane injection. n = 7 for each genotype. **B** Representation and quantitation of CD206⁺ cells among AMs. Quantification is shown as a percentage of indicated immune cells among AMs⁺ cells. n = 7 for each genotype. **C** Expression of MHCI, CD206 and CD11c and frequency of CD80 in the CD11c⁺ IM population. n = 7 for each genotype. **D** Frequencies of B (B220⁺ NK1⁻), CD4⁺, CD8⁺ NK1.1⁺ cells among CD45⁺ cells, expression of CD44 on CD8⁺ cells and frequency of activated NK1.1⁺ cells (B220⁺) among NK1.1⁺ cells. n = 7 for each genotype. Data were analyzed by unpaired t-test.

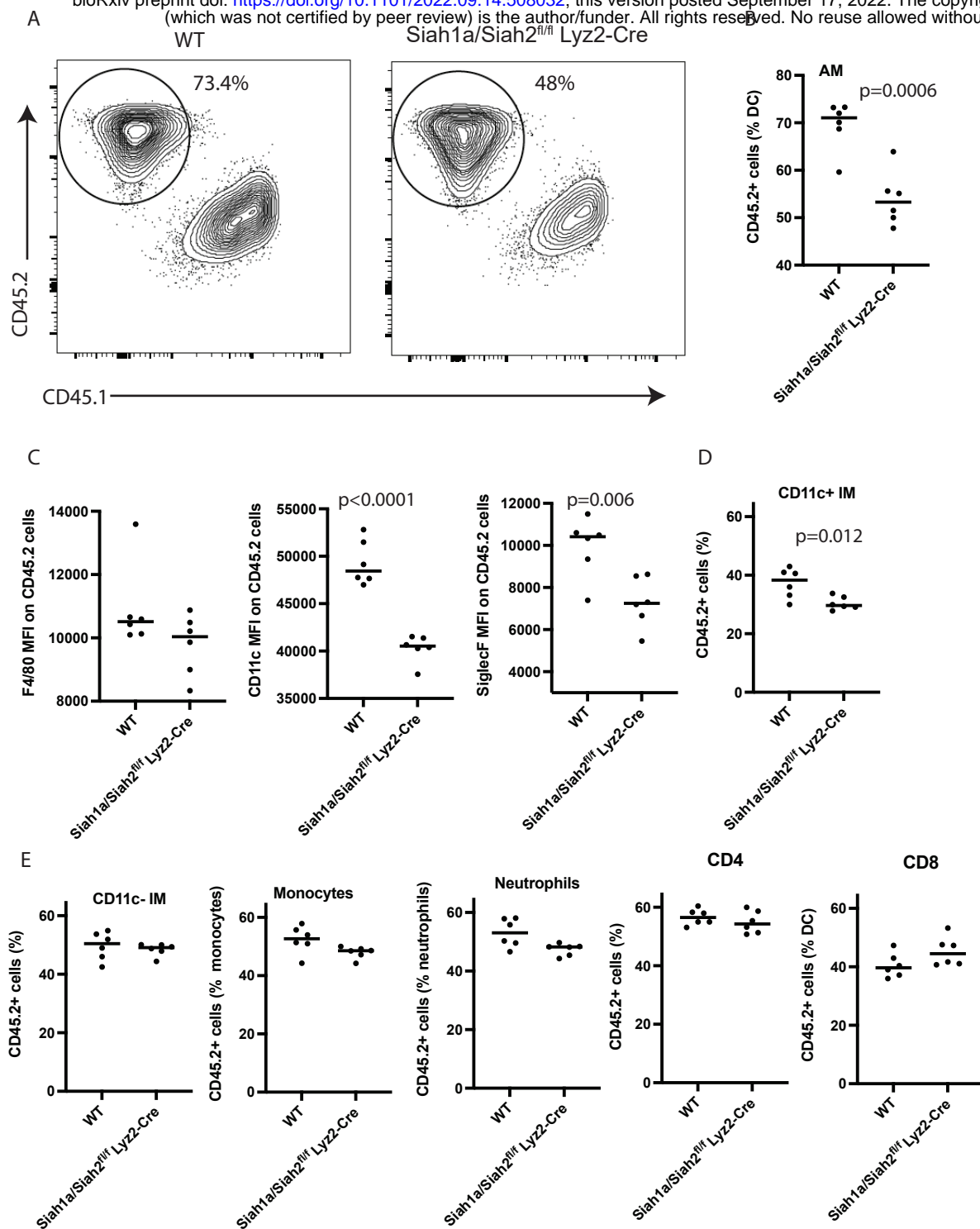
Sup. Figure 5. Single cell RNA-seq analysis of CD45⁺ cells in lungs of urethane-treated mice. CD45⁺ cells were sorted by flow cytometry from WT and *cSiah1a/2^{ff}::Lyz2^{Cre}* lungs collected 7 weeks after the first urethane injection, and single cell RNA-seq was performed. **A** Table showing the proportion of cells in each cluster within CD45⁺ clusters from WT and *cSiah1a/2^{ff}::Lyz2^{Cre}* CD45⁺ cells, related to UMAP in Figure 6A. **B** Violin plots comparing expression levels of select genes from cluster 5 (macrophages). **C** UMAP plots showing expression of NRF2 in all CD45⁺ cell clusters. Data in panel B were analyzed using *FindMarkers()* and *MAST* test in Seurat.

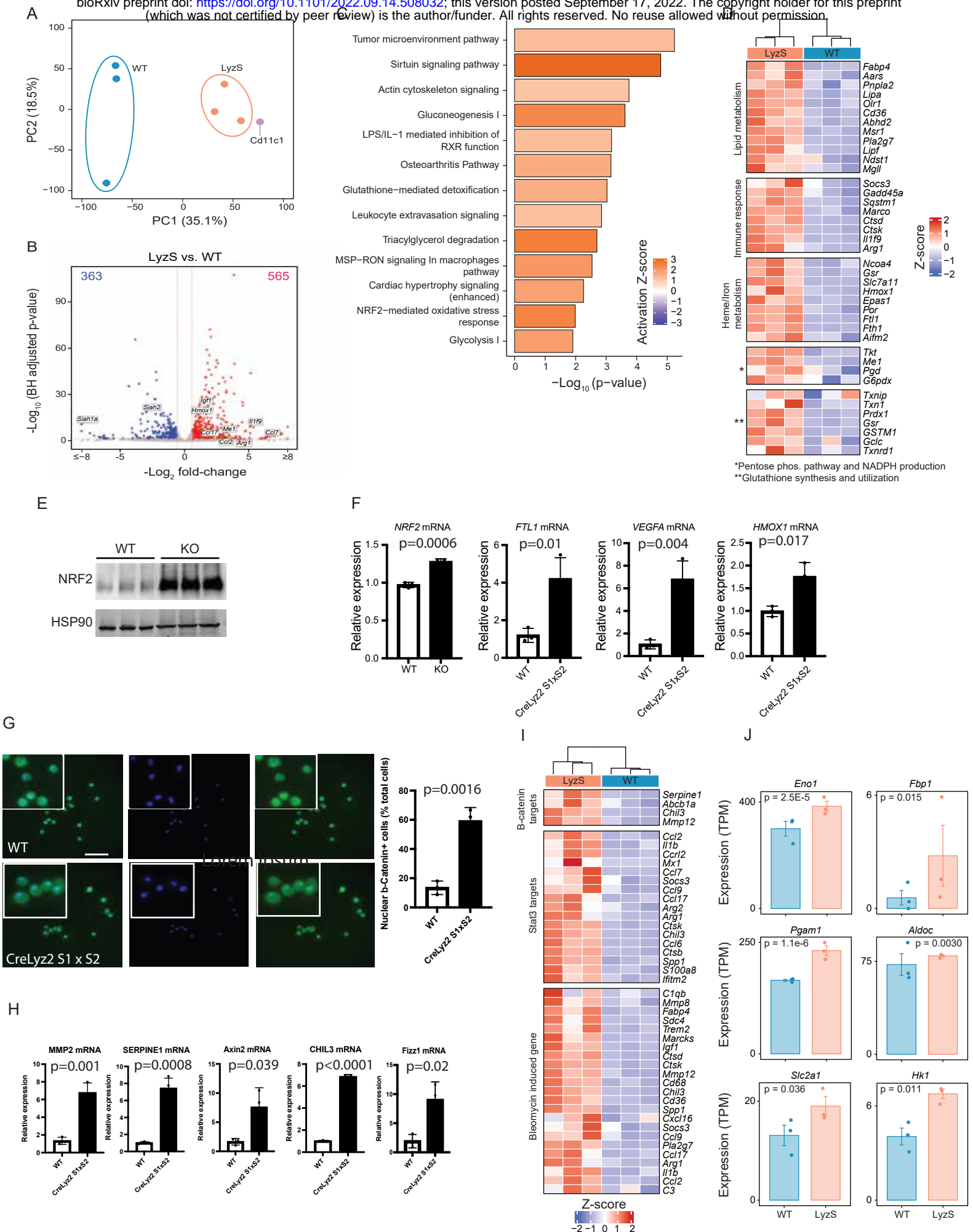
Sup. Figure 6. Single cell RNA-seq analysis of myeloid cells in lungs of urethane-treated mice. Clusters 2, 3 and 5 from single cell RNA-seq analysis of CD45⁺ cells (Figure 6A) containing myeloid cells were re-clustered to provide higher resolution clustering into 8 new clusters. **A** Table representing the proportion of cells within each myeloid cell cluster from WT and *cSiah1a/2^{ff}::Lyz2^{Cre}* cells. **B** Violin plots comparing expression of select

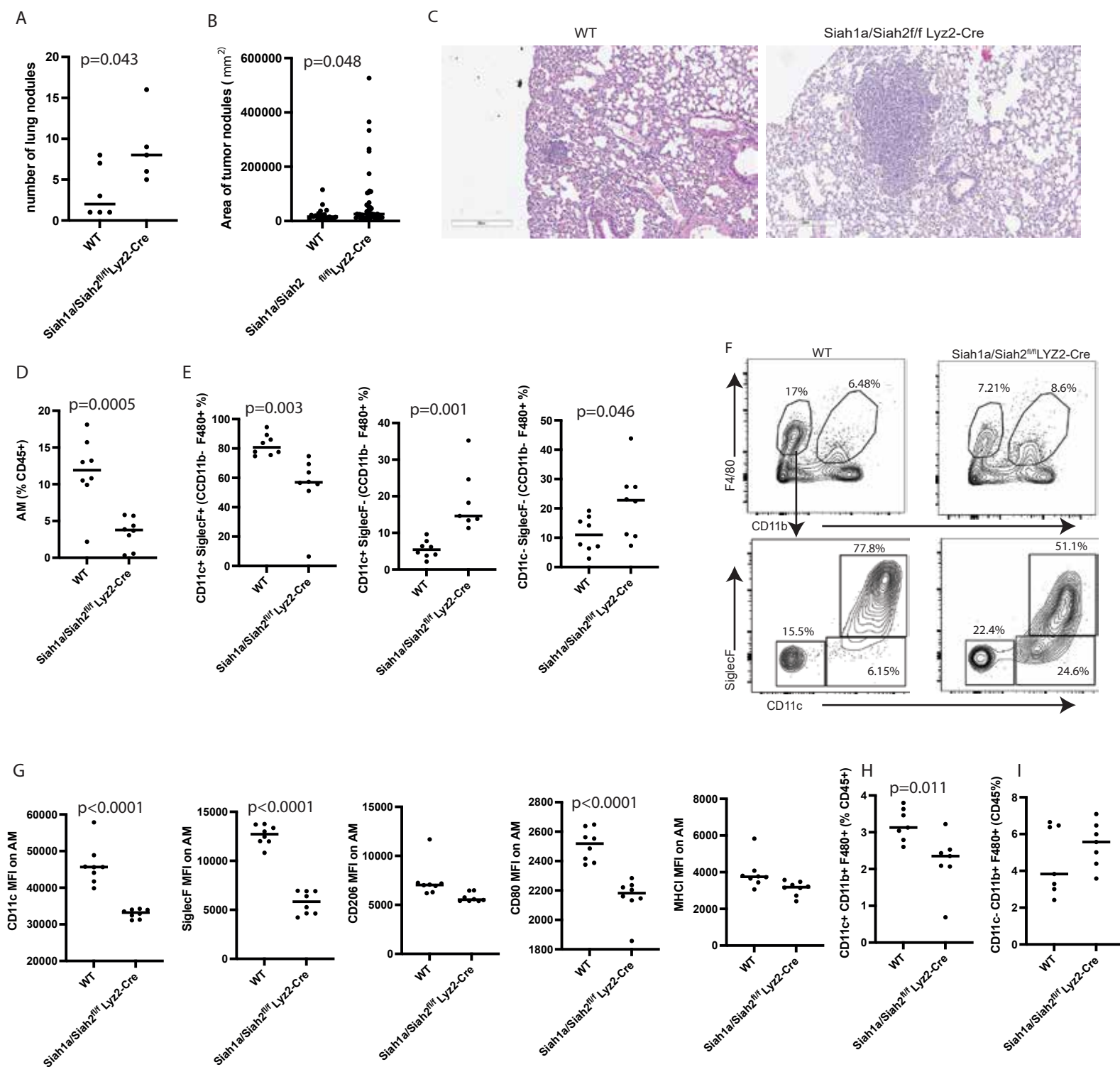
genes from sub-cluster 0 in myeloid cells. **C** Frequencies of LY6C⁺ cells among mature AMs, immature AMs (CD11c⁻ SiglecF⁻ CD11b low and F480⁺ and CD11c⁺ SiglecF⁻ CD11b low and F480⁺), CD11c⁺ IMs and CD11c⁻ IMs in lungs at 22 weeks after urethane injection. n = 6 for each genotype. **D** 72 Inflammatory genes significantly upregulated in myeloid sub-cluster 0 of Siah1a/2-deleted cells relative to WT were used to calculate hazard ratios in the TCGA-LUAD patient cohort. For each gene, the cohort was stratified as high and low expressors using optimally best cutoff. Shown are hazard ratios, 95% confidence intervals, and p-values (log-rank test). Data in panel B were analyzed using *FindMarkers()* and *MAST* test in Seurat, data in panel C were analyzed by unpaired t-test.



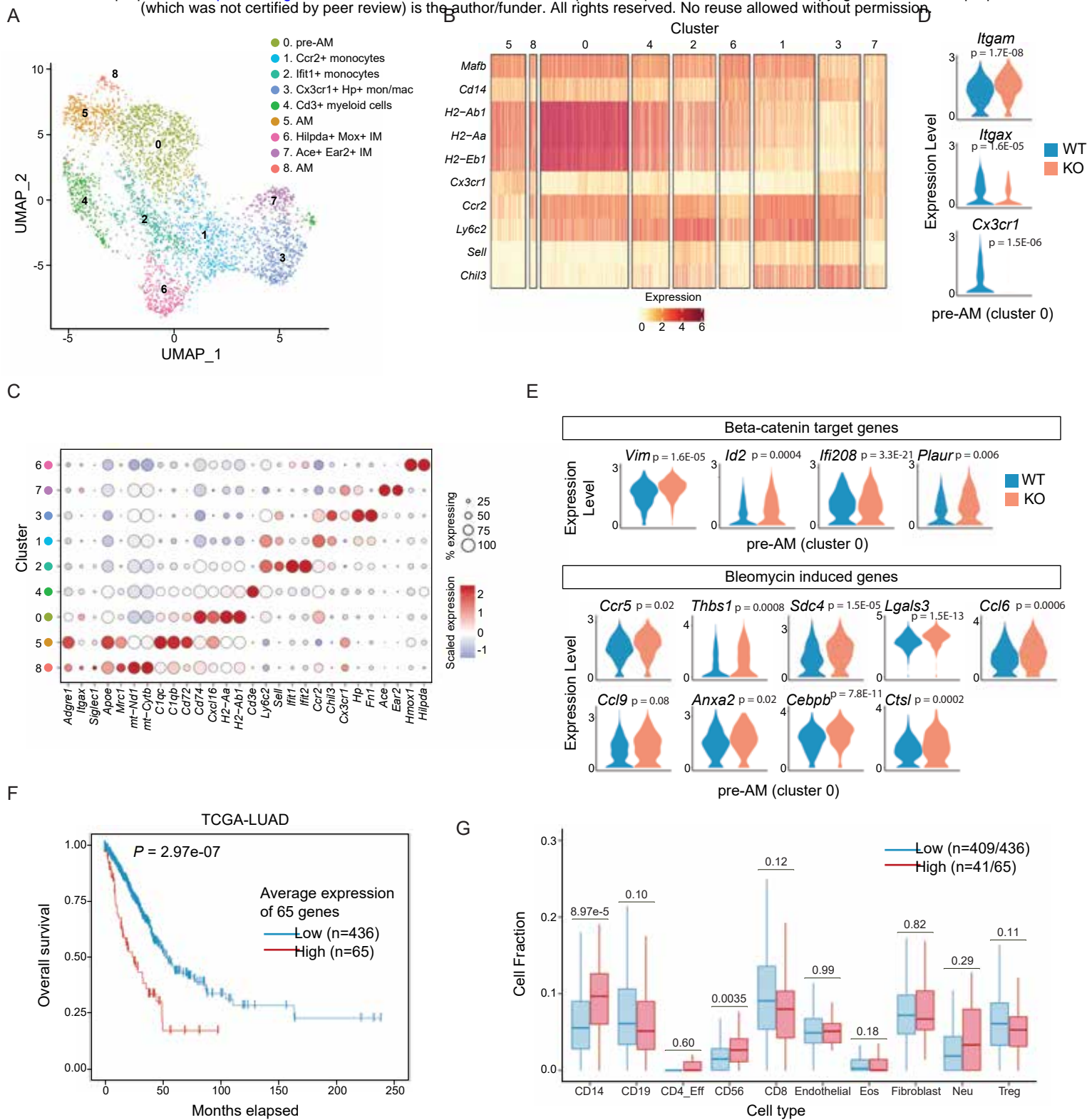


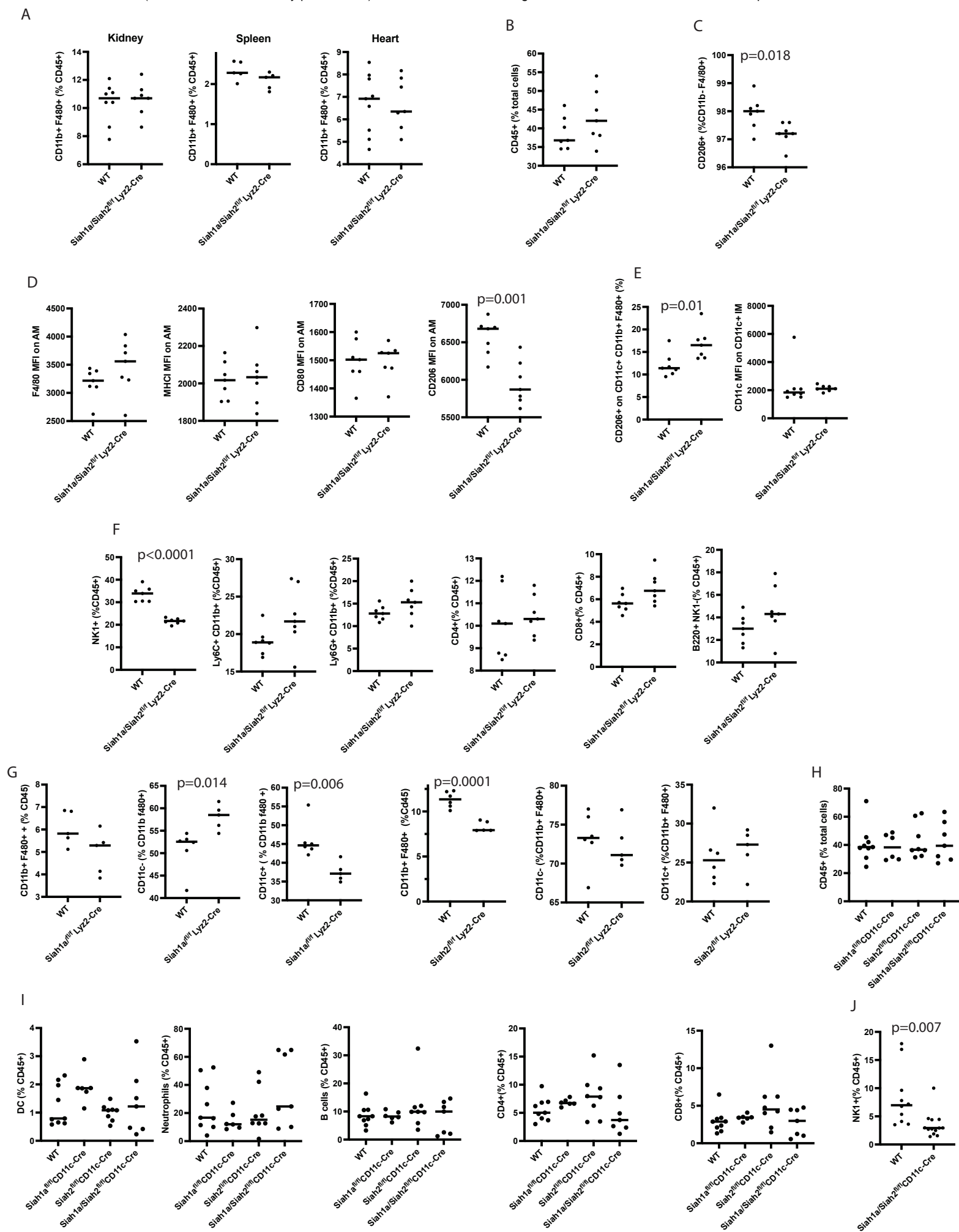


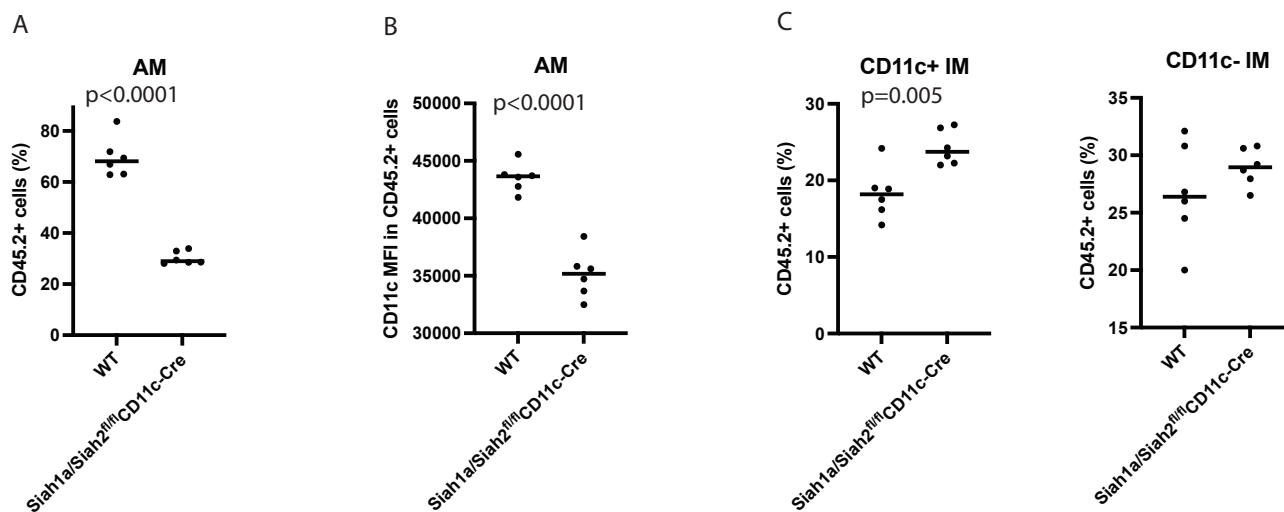




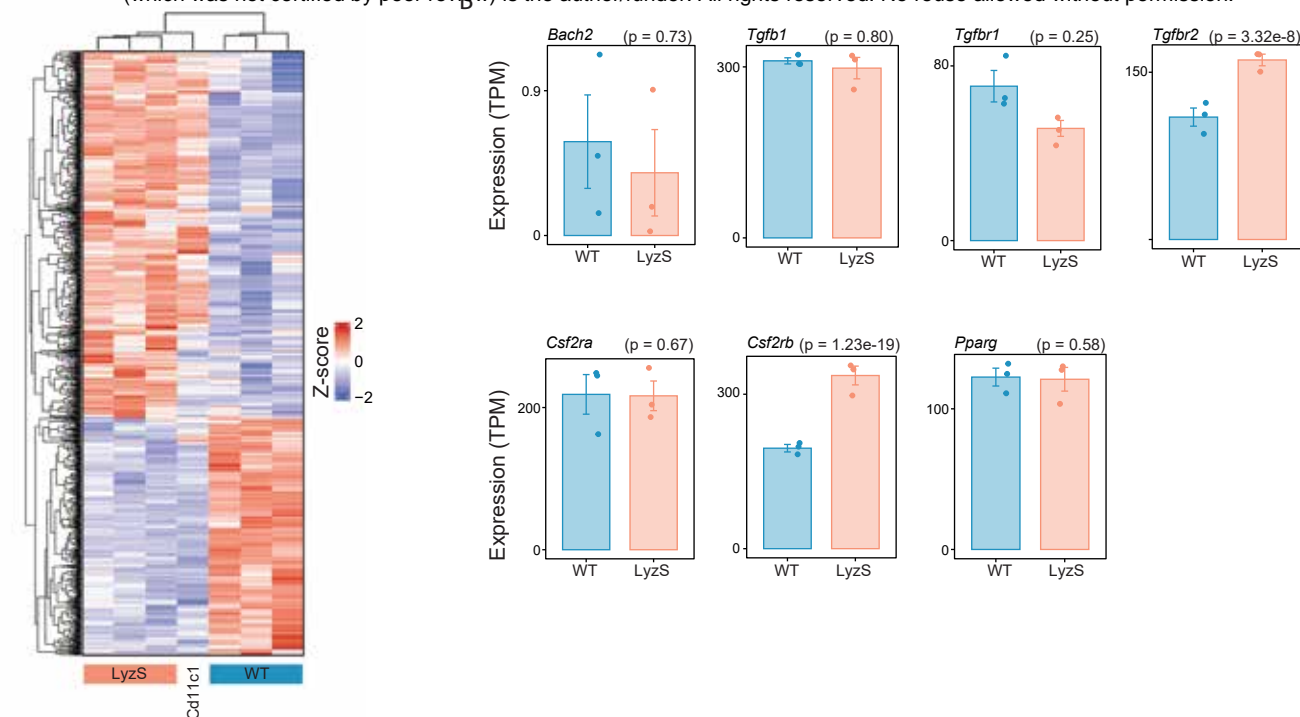




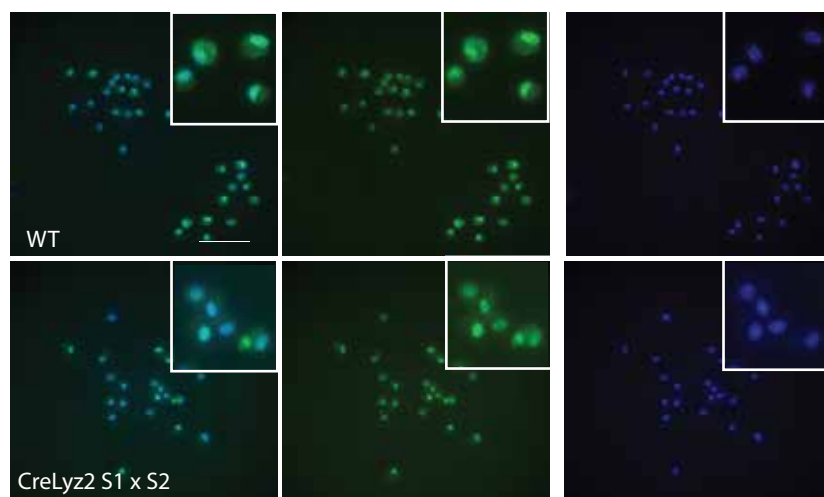




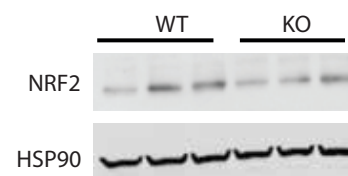
A



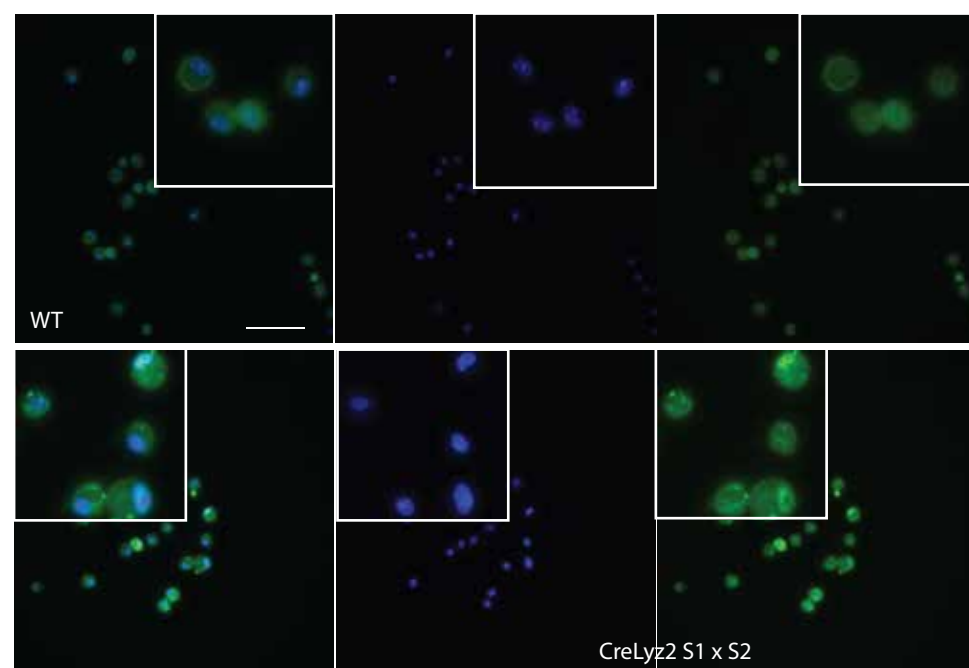
C

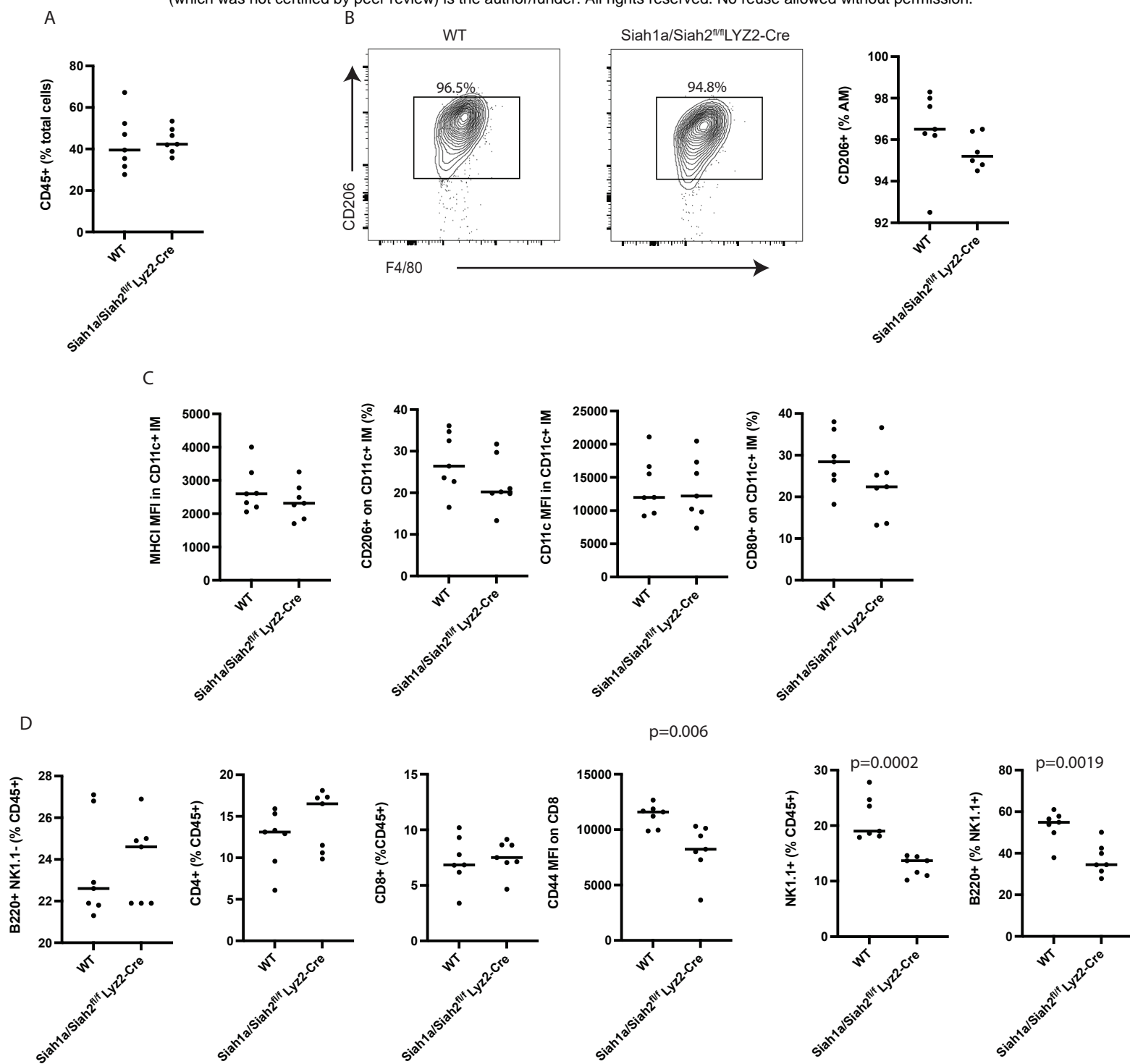


D



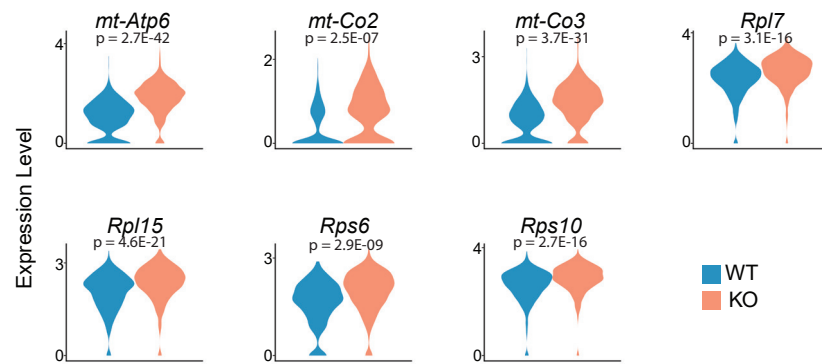
E



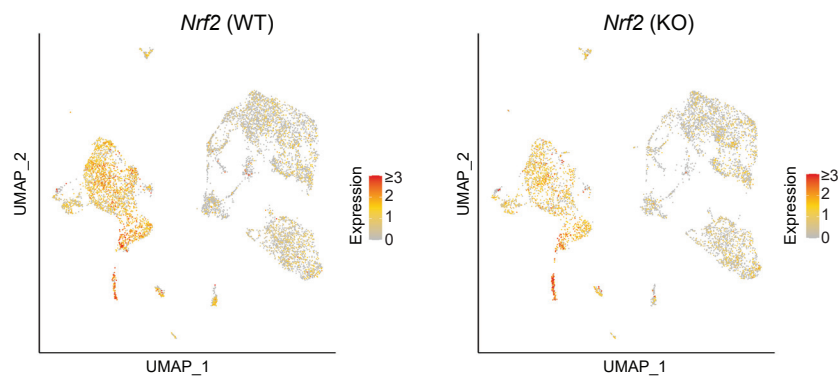


A

Cluster	KO (% CD45)	WT (% CD45)
0	20.65	16.83
1	16.36	14.12
2	9.52	11.14
3	7.66	10.37
4	4.32	5.60
5	4.69	4.83
6	5.03	3.61
7	3.92	4.12
8	3.83	4.06
9	3.95	3.93
10	2.93	4.46
11	2.82	3.73
12	2.75	1.15
13	1.76	1.48
14	1.28	1.02
15	0.79	1.26
16	0.88	0.81



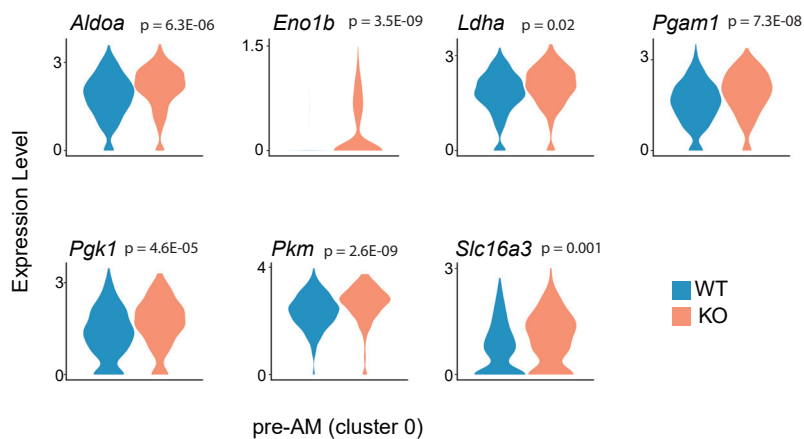
C



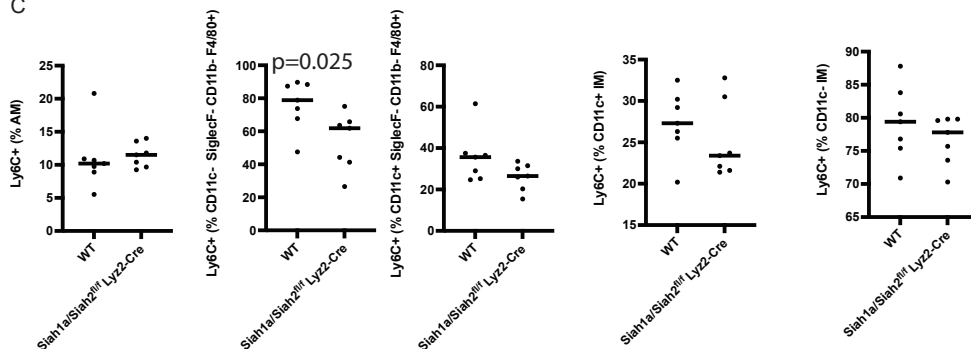
A

	% CD45+	
Cluster	KO	WT
0	5.4	6.3
1	3.7	4.4
2	2.6	3.0
3	2.7	2.8
4	2.8	2.3
5	1.8	2.7
6	1.0	2.8
7	1.5	1.5
8	0.4	0.5

B



C



D

